

Application of Advanced Surface Imaging and Image Analysis for Biotechnological Drug Development.

Master's Thesis in Pharmaceutical Development

AMANDA LARSSON

Department of Chemistry

CHALMERS UNIVERSITY OF TECHNOLOGY
Gothenburg, Sweden 2026
www.chalmers.se

MASTER'S THESIS IN PHARMACEUTICAL INDUSTRY

Application of Advanced Surface Imaging and Image Analysis for Biotechnological Drug Development.

AMANDA LARSSON



Department of Chemistry
CHALMERS UNIVERSITY OF TECHNOLOGY
Gothenburg, Sweden 2026

Integrating SEM–EDX and ToF-SIMS for Correlative Elemental–Molecular Imaging: Workflow Development, Stage-Tilt Alignment, Charge Management, and Reference-Based Analysis Applied to Pharmaceutical formulations and Ex Vivo Skin Models.

AMANDA LARSSON

@ AMANDA LARSSON, 2026.

Supervisor: Anna Olsson, Eleonora Paladino, Mats Josefson & Mats Hertel
(AstraZeneca)

Collaborator: Gabriele Colcerasa and Ioannis Andreadis (AstraZeneca)

Examiner: Per Malmberg (Chalmers).

Master's Thesis 2026
Department of Chemistry
Chalmers University of Technology
SE-412 96 Gothenburg, Sweden
Telephone + 46 31 772 100



High-magnification image of the spray-dried protein powder, highlighting intra-sample variability in particle size, surface topography, and morphology.

Gothenburg, Sweden 2026

Integrating SEM–EDX and ToF-SIMS for Correlative Elemental–Molecular Imaging: Workflow Development, Stage-Tilt Alignment, Charge Management, and Reference-Based Analysis Applied to Pharmaceutical Powders and Ex Vivo Skin Models

AMANDA LARSSON

Department of Chemistry
Chalmers University of Technology

Abstract

This M.Sc. thesis presents a correlative imaging workflow that integrates high resolution scanning electron microscopy (SEM) imaging and energy dispersive X-ray (EDS/EDX) elemental mapping with time-of-flight secondary-ion-mass spectrometry (ToF-SIMS) molecular analysis to interrogate composition and microstructure within shared regions of interest. The approach was implemented on pharmaceutical powders, including a spray-dried powder containing proteins and an excipient blend as well as an ex vivo human skin model exposed to $AlCl_3$. Coordinated acquisition and harmonized processing enabled co-registration of elemental and molecular signals, improving interpretation of interfaces and component distributions compared with single-modality analyses. Practical aspects of implementation were examined in detail, including substrate choice, stage-tilt alignment due to differences in acquisition angles across instruments, charge management (variable-pressure operation), and image registration between the outputs of multivariate analysis (MVA) of ToF-SIMS hyperspectral images and the corresponding SEM fields of view. Limitations encountered during this study, such as the need for validated reference materials in complex matrices and vacuum mode switch inducing field-of-view shifts, were documented alongside mitigations and recommendations for routine use. The results demonstrate that the combined SEM–EDX and ToF-SIMS strategy can deliver complementary insights across disparate sample types, and they outline future refinements to enhance reproducibility and throughput, including standardized tilt protocols, expanded reference libraries, and improved registration algorithms. Overall, the thesis establishes a practical foundation for applying correlative imaging workflow in pharmaceutical contexts and highlights its potential for broader materials and biological applications.

Preface

This report describes a master's thesis (30 credits) conducted at AstraZeneca from January to June. The project was supervised by Anna Olsson, Eleonora Paladino, Mats Josefson, and Mats Hertel at AstraZeneca, with additional support from collaborators Gabriele Colcerasa and Ioannis Andreadis. The project was examined by Per Malmberg, Associate Professor at Chalmers University of Technology.

Acknowledgments

The individual project and the work conducted at AstraZeneca was made possible through the support of many people. I would like to express a big thanks to my supervisors Anna Olsson, Eleonora Paladino, Mats Josefson and Mats Hertel for their mentorship throughout the project and helping me achieve an easy and welcoming onboarding to AstraZeneca and the Material Design group. They have been of great support with the thesis but also with helping me to navigate questions and broadening my vision on the product development process. I am especially grateful to Anna Olsson for her support with the SEM-EDX work and the surrounding aspects, and to Eleonora Paladino for her guidance and support on the ToF-SIMS. Both Mats Josefson and Eleonora Paladino were of great help with learning ImagePipeline throughout this thesis.

I also thank Gabriele Colcerasa and his supervisor Ioannis Andreadis for their collaboration during this project, including valuable brainstorming and fresh perspectives. An even bigger gratitude for Gabrieles work within this thesis, creating and building a computer model for the overlaying and registration of the images from ToF-SIMS and SEM-EDX. This has been very useful to bring the correlative workflow together.

Furthermore, I would like to thank my examiner at Chalmers, Per Malmberg, for ensuring that the project meets the academic requirements and for his support throughout, which helped the work proceed smoothly. As well as collaborations and ideas being discussed with Per Malmberg and Jonas Sjöblom for future development of the correlative workflow.

Table of Contents

Abstract 5
Preface 6
Acknowledgments 6
Table of Contents 7
List of figures 10
List of tables 11
1. Introduction 12
1.1 Background 12
1.2 Previous research 13
1.3 Purpose and objective 14
1.4 Demarcations 15
2. Theory 16
2.1 Pharmaceutics 16
2.1.1 History 16
2.1.2 Pharmaceuticals 16
2.1.5 Excipients 17
2.1.6 Blending 17
2.1.7 Spray drying 18
2.1.8 Ex vivo skin model 18
2.2 Techniques 18
2.2.1 Scanning electron microscopy 18
2.2.2 Energy dispersive X-ray spectroscopy 20
2.2.3 Sputter Coater 21
2.2.4 Time of Flight – Secondary Ions Mass Spectrometry 22
2.2.5 M6 Hybrid SIMS (OrbiSIMS) 24
2.2.6 PMA 24
2.2.7 ImageJ 24
3. Method 25
3.1 Sample preparation 25
3.1.1 PMA stock solutions 25
3.1.2 Sample preparation for samples used for evaluating SEM and ToF-SIMS parameters 25
3.1.3 Sample preparation for optimization of tilting angles within SEM-EDX 26
3.2 Method optimization of SEM-EDX 27
3.2.1 Acceleration voltage 27
3.2.2 Variable pressure mode 28
3.2.3 Working distance 28

3.2.4 PMA thickness 28
3.3 ToF-SIMS methodology 29
3.3.1 Setting up the instrument 30
3.3.2 PMA thicknesses 30
3.3.3 Composition analysis of excipient blend and spray-dried powder 30
3.3.4 ImagePipeline 31
3.4 Image location and Registration 31
3.4.1 Creating markings for finding the same image location 31
3.4.2 Optimization of angles within the instrument 32
3.5 Applying the correlative workflow 35
3.5.1 Spray-dried powder with protein 35
3.5.2 Excipient blend 36
3.5.3 Ex vivo human skin exposed to $AlCl_3$ 36
4. Results 37
4.1 Factors in SEM-EDX 37
4.1.1 Acceleration voltage 37
4.1.2 Variable pressure mode 40
4.1.3 Working distance of EDX detector 41
4.1.6 PMA thickness 42
4.2 ToF-SIMS 44
4.2.1 Evaluation of PMA thickness 44
4.2.2 Peak identification and compositional mapping with IONTOF software 45
4.2.3 ImagePipeline 47
4.3 Image location 47
4.3.1 Creating markings for finding the same image location 47
4.3.2 Optimization of acquisition angles within the instruments 49
4.3.3 Image Registration 50
4.4 Applying the correlative workflow 50
4.4.1 Spray dried powder with protein 50
4.4.2 Excipient Blend 52
4.4.3 Ex vivo human skin exposed to $AlCl_3$ 54
5. Discussion 56
5.1 Method optimization 56
5.1.1 SEM-EDX 56
5.1.2 ToF-SIMS 56
5.2 Correlative workflow 57
5.2.1 Build of the correlative workflow 57

5.2.2 Applying the correlative workflow 58
5.2.3 Challenges 59
5.2.4 Benefits 60
5.3 Further evaluation and prospects 61
6. Conclusion 64
Bibliography 65
Appendix 71
A1: Excipient blend 71
A2: ImageJ to quantify charging on imaged surface. 71
A3: Correction of measured pixels from ImageJ 72
A4: Example calculations of charging% from ImageJ output 72
A5: Placement of sample in SEM holder 74
A6: Images of CP before and after EDX at different acceleration voltages 75
A7: Elemental maps Excipients on PMA C at 5 kV 76
A8: Elemental maps Excipients on PMA C at 15 kV in VP mode 77
A9: Elemental composition of spray-dried powder at different kV in VP mode 78
A10: Elemental composition of cluster on AP sample at different working distances 78
A11: Elemental composition of different PMA thicknesses at 3 kV 79
A12: Visual Observation of the charging on PMA A (AP) and PMA E (EP) at 5 kV 79
A13: Different angles evaluated with SEM 79
A14: Elemental maps of the skin model (SEM-EDX) 81

List of figures

Figure 1: Schematic illustration of the scanning electron microscope 18
Figure 2: Schematic illustration of the components included in ToF-SIMS..... 22
Figure 3: Samples used to evaluate PMA thickness; image generated by AI. 26
Figure 4: Illustration of the SEM method used to measure PMA thickness. 29
Figure 5: Schematic of image locations relative to the added fiducial craters. 32
Figure 6: Image Registration SEM + SIMS..... 33
Figure 7: Image registration of EDX electron image onto SEM coordinates..... 34
Figure 8: Charging accumulation over different acceleration voltage (2-4 kV)..... 37
Figure 9: Quantified charging (%) at three acceleration voltages. 38
Figure 10: SEM image showing charging at 2 kV in the spray-dried powder. 39
Figure 11: Elemental maps of sodium (Na) at different vacuum modes and acceleration voltages. 40
Figure 12: SEM images of the spray-dried powder across accelerating voltages (VP mode). 41
Figure 13: Elemental map overlay for sample AP at two working distances. 42
Figure 14: Quantified charging (%) of samples at different accelerating voltages..... 43
Figure 15: Excipient blend on substrate PMA A (AP). 44
Figure 16: Excipient blend on substrate PMA E (EP). 44
Figure 17: Spray-dried material on PMA A. 45
Figure 18: Spray-dried material on PMA E. 45
Figure 19: Overlay of excipient distributions on PMA E. 46
Figure 20: Component-identified overlay of spray-dried powder on PMA A. 46
Figure 21: Component prediction overlays (SSG, MgSt, MCC, DCPA, PMA) generated by ImagePipeline. 47
Figure 22: Fiducial craters observed in excipient samples at different PMA thicknesses. 48
Figure 23: Image locations across SEM and ToF-SIMS datasets. 48
Figure 24: Side-by-side comparison of image angles in SEM and ToF-SIMS. 49
Figure 25: Multimodal image registration and composite overlay. 50
Figure 26: Multimodal registration of the 5% BSA spray-dried powder. 51
Figure 27: Multimodal registration of the 10% BSA spray-dried powder. 51
Figure 28: Multimodal registration of the 20% BSA spray-dried powder. 52
Figure 29: Multimodal image registration of the Excipient blend. 53
Figure 30: SkinModel images obtain from both ToF-SIMS and SEM. 54
Figure 31: EDX elemental maps registered onto the high-resolution SEM image..... 55
Figure 32: Elemental density per component for different acquisition times. 62
Figure 33: Mireg output with filtered Mg elemental map 62

List of tables

Table 1: Overview of PMA dilutions setups 25
Table 2: Starting parameters for EDX acquisition. 27
Table 3: Thresholds used to quantify pixels exhibiting charging effects. 27
Table 4: Protocol for achieving comparable image quality across all PMA thicknesses 29
Table 5: Selected threshold for counting pixels exhibiting charging artifacts. 29
Table 6: EDX elemental weight% detected at different acceleration voltages. 38
Table 7: Elemental composition in high-vacuum (5 kV) and variable-pressure (10 kV) SEM: a comparison. 40
Table 8: Different settings for the analysis of how and if working distance influences the EDX analysis. 42
Table 9: Summary of mean thickness and ranges for PMA solution. 43
Table 10: Color assignment for each component. 46

1. Introduction

1.1 Background

Modern biotechnology is transforming pharmaceutical development, with biologically derived drugs such as proteins, peptides and nucleic acid therapeutics. As these biological components are incorporated into pharmaceutical formulations, a key challenge is understanding how microstructure and surface properties influence the stability, integrity, and bioavailability of sensitive macromolecules, as well as their safety and immunogenicity risk. Advanced analytical imaging techniques, such as Scanning Electron Microscopy with Energy-Dispersive X-ray analysis (SEM-EDX) and Time-of-Flight Secondary Ion Mass Spectrometry (ToF-SIMS), offer high spatial and molecular resolution to characterize surface composition and map how component distributions affect product performance.

In pharmaceutical product development, many aspects such as formulation development and process development require evaluation. One key process is spray drying, a method that converts solutions or suspensions into dry powders to improve delivery and stability of the drug substance. During drying, the spatial distribution of components can change; analyzing these changes is essential because they can lead to enrichment of certain components at the particle surface (1). Excipients with low aqueous solubility or high surface activity can preferentially migrate to the surface and form a continuous surface layer or film (often referred to as surface-active excipients or film-forming excipients), which stabilizes the particle core. Spray drying has strong potential for products that contain biological components such as proteins and oligonucleotides. These components are fragile, and spray drying can help preserve their activity by enabling controlled, rapid drying. Understanding the properties of spray-dried powders is critical for enabling controlled deposition and release of drug substances in patients.

By combining SEM-EDX and ToF-SIMS, pharmaceutical development teams can answer questions concerning the identity, spatial distribution and chemical composition of features within complex pharmaceutical samples. Together, these methods reveal compositional gradients across interfaces and coatings and directly link microstructure to composition. The techniques are complementary: SEM-EDX provides high-resolution imaging with site-specific elemental analysis, whereas ToF-SIMS delivers molecular information via mass spectrometry with exceptional surface sensitivity. Their differences in analysis depth make them synergistic for understanding surface and near-surface features in pharmaceutical formulations.

These techniques are particularly valuable for investigating how biotechnological production methods, formulation strategies, and interactions influence the performance of biopharmaceutical products. Applying SEM-EDX and ToF-SIMS to relevant biologic-containing samples enables insights that support the rational design and optimization of next-generation biopharmaceuticals.

1.2 Previous research

Both analytical techniques, SEM-EDX and ToF-SIMS, have been used for a long time in many different fields. Both techniques are based on surface analysis. In previous research both techniques have been used to analyze organic, inorganic as well as biological samples, showing a broad usage of the two techniques. The results have varied, and certain changes needed to be made to optimize the technique for a specific sample. For example, earlier ToF-SIMS studies have shown it can tell apart amorphous areas from re-crystallized areas in single-compound amorphous samples. It has also been shown to work efficiently in characterizing Active Pharmaceutical Ingredients (API) (2) (3).

Using ToF-SIMS for biological samples, different protocols have been developed which can be followed depending on the biological sample and on the water content, among other properties (4) (5). For SEM-EDX there are fewer published articles where biological samples have been used. Biological samples such as tissues and cells are often analyzed with low voltage SEM (6). There are also examples where sputtering has been used during sample preparation to add a conductive layer on top of the sample. Sputtering can be used for biological samples due to tissues and cells being sensitive to electrons, which can damage the structure of the sample (7).

There have also been studies using both SEM-EDX and ToF-SIMS to retain as much information of a sample as possible, showing that there is a good correlation between the two techniques (8) (9). For instance, EDX can be performed prior to ToF-SIMS to verify sample morphology and elemental features (10) (11) (12). In another article, ToF-SIMS is employed when EDX approaches its limits in terms of detectable concentration and lateral resolution, thereby extending the chemical insight beyond what EDX can provide (8).

The combined use of ToF-SIMS and SEM-EDX extends beyond pharmaceutical development. One study demonstrated a complementary workflow for the investigation of cement-based materials, showing that this approach is particularly effective for detecting compounds present at low concentrations, where EDX suffers from a poor signal-to-noise (S/N) ratio (8). Another study highlighted the value of combining these techniques by leveraging ToF-SIMS to obtain in-depth 3D chemical information, thereby providing spatially resolved molecular insight that EDX alone cannot deliver (11).

Several evaluations have applied ToF-SIMS and SEM-EDX in parallel to cross-validate findings related to sample morphology, chemical specificity, and feature size. Together, the datasets provide complementary and valuable information about the components present in the sample. While the identification of elements is generally consistent between the two techniques, ToF-SIMS offers enhanced molecular-level detail, including insights into the molecular formula and specific ion species, which can strengthen the interpretation of chemical composition and support more robust conclusions (9) (11) (13).

One research developed a correlative workflow and quantification strategy combining ToF-SIMS and SEM-EDX by using Kirkendall voids as location markers (12). These voids enabled both techniques to target the same region, making direct location-matched comparisons possible. Because Kirkendall voids are specific to certain material systems, they are not suitable as localization markers for the samples in this thesis. Nevertheless, the study demonstrates that co-registering ToF-SIMS and SEM-EDX at identical locations is possible and can clarify the complementary information each technique provides. The same study reported that differences in sequencing depth between ToF-SIMS and SEM-EDX did not affect the conclusions for the specific sample examined. However, depth-related considerations may still be relevant for certain particle types, where the chemical composition can vary with depth and thus influence the interpretation of correlative analyses (12).

Another article used a correlative workflow between the two techniques to identify uranium particles: SEM-EDX was used first for the identification and location coordinates before performing focused ion beam time of flight secondary ion mass spectrometry (FIB-ToF-SIMS) and large geometry secondary ion mass spectrometry (LG-SIMS). SEM was also used for morphology, where the FIB-ToF-SIMS was further used for identifying the isotopic composition (10).

The outputs from the two techniques can be used independently or integrated. In one study on image fusion, researchers combined the high-resolution morphology from SEM with the lower-resolution image and chemical maps from ToF-SIMS to generate a hybrid image that preserves the chemical specificity of ToF-SIMS while achieving the spatial resolution of SEM (14). In addition, a separate publication reported data fusion approaches that integrate SEM-EDX and ToF-SIMS datasets to enhance interpretability and quantitative insight (15).

1.3 Purpose and objective

The aim of this project is to apply SEM-EDX and ToF-SIMS to characterize the surface and microstructural properties of biotechnologically relevant pharmaceutical formulations. Special emphasis will be placed on formulations containing biological components such as proteins, and on biological tissue samples.

The project seeks to:

- Develop a correlative workflow between SEM, EDX and ToF-SIMS.
- Use image analysis software to analyze and correlate the images obtained from SEM-EDX and ToF-SIMS.
- Gain knowledge from SEM-EDX and ToF-SIMS for the characterization of pharmaceutical active ingredients, formulations and biological tissue samples.
- Use SEM-EDX and ToF-SIMS to assess the distribution of biological components within solid formulations.

1.4 Demarcations

This project includes specific scope limitations due to time and resource constraints.

- The project was conducted at AstraZeneca. To respect confidentiality, detailed molecular identities, proprietary compositions, and exact structures will not be disclosed. Instead, descriptions will use general, widely recognized terminology for compounds and materials.

- The specific choice of biological samples and formulations was determined based on available resources and ongoing discussions with industrial and academic partners.

- To establish a complete workflow that includes image registration and analysis of the acquired data, a computer program was developed by Gabriele Colcerasa, Graduate Scientist at AstraZeneca. This tool uses the findings of this thesis to generate relevant outputs for the development unit.

2. Theory

2.1 Pharmaceutics

2.1.1 History

The pharmaceutical industry focuses on the discovery, development, and manufacture of drugs and medications. The oldest record of preparations of medicines is from the early 28th century BC. During this time, it was mostly plants, animals or minerals used for treating various conditions. Moving forward in time until around middle of 16th century, when the first pharmacopoeia appeared in Germany, it was the first collected list of drugs and medicinal chemicals. This inspired many more countries, and the next milestone happened in England in 1618 when the first national pharmacopoeia was published and mandatory for the whole of England (16).

Moving into the 17th century many milestones were covered, the first being the first isolation of compounds such as morphine. This led to the possibility of accurate dosage which could be administered, due to the extraction of the compounds. After it became possible to extract the compounds, scientists and researchers could receive knowledge about the chemical structure of the drugs leading to the possibility of laboratory synthesis (16).

The pharmaceutical industry experiences a substantial expansion through the 19th and 20th century due to several important new classes of pharmaceuticals being developed, as well as several changes in the discovery, development and manufacturing took place (16).

2.1.2 Pharmaceuticals

Pharmaceuticals are defined as substances used for treatment, prevention and diagnosis of diseases. The pharmaceuticals are classified by their chemical group, pharmacological effect and by their usage (17).

In the development of a pharmaceutical product, it is important to study the drug delivery system. The aspects of the 3D structures as well as their interaction with the organism taking the pharmaceutical. It is important to determine how it interacts with the organism's physiological structure and if it has a likelihood of being functional in view of the kinetic and target abilities of the active pharmaceutical ingredient (17).

The active pharmaceutical ingredient (API) is also known as a drug substance. It is the primary component of a pharmaceutical product which provides the intended therapeutic effect (18) (19). The physical and chemical properties of the API are important for its therapeutic effect as well as the bioavailability of the compound. Primary properties include particle size distribution, crystal form, morphology, surface area, solubility and stability. These factors play a major role in the bioavailability and therapeutic effects as well as the overall absorption (20).

2.1.5 Excipients

Pharmaceutical products must include an active pharmaceutical ingredient (API), but they are not composed of the API alone. Instead, it also contains different excipients which are the inactive ingredients in a drug product. These excipients have important properties which influence the role in formulation of pharmaceuticals (21). Excipients have the important role to protect, stabilize, deliver, increase and enhance the compliance of the drug. Excipients can also improve the bioavailability of the API. For example, excipients can act as binders, lubricants, plasticizers and more (22). There are many different excipients, but the ones used in this study are magnesium stearate, microcrystalline cellulose, dicalcium phosphate anhydrous and sodium starch glycolate.

Magnesium stearate (MgSt) is an excipient that consists of the magnesium salt of steric acid. In pharmaceuticals MgSt is commonly used as a lubricant, meaning it helps to avoid that the material sticks to the processing equipment (23) (24). Microcrystalline cellulose (MCC) is another common excipient used in the pharmaceutical industry. MCC is mostly used as a binder, disintegrant, bulking agent or diluent (25). MCC is obtained by hydrolytic depolymerization of cellulose to enhance and isolate the crystalline regions. The properties of MCC affect the hardness and dissolution of the pharmaceutical product. (24).

Dicalcium phosphate is an excipient which can have two forms: anhydrous and dihydrate. The anhydrous form DCPA has a triclinic crystal structure (24), i.e. its structure consists of a 3D network of phosphate ion tetrahedral with calcium ions bound together by ionic bonds with oxygen (26). DCPA is widely used as a binder and filler in pharmaceutical products, due to the properties such as flowability and compressibility characteristics (27). Sodium starch glycolate (SSG) is the sodium salt part of the carboxymethyl ether of starch, which is a polysaccharide consisting of amylose and amylopectin. To form SSG the starch goes through two chemical modifications, of which one being substitution, which affects the properties of SSG. The resulting SSG is a super disintegrant, belonging to a group of excipients that has a rapid swelling in contact with water resulting in fast disintegration of e.g. tablets. (24) (28).

2.1.6 Blending

In the pharmaceutical industry, a combination of components is often used in the formulation of drug products. During the process of combining, blending is a very important unit operation as it is responsible for the homogenous distribution of the API in the drug product (29). Blending is influenced by the specific components and their ratios as excipients have different characteristics and properties. Blending also depends on parameters such as process time, mixing time, blending speed. In the final product it is important that the blend is homogenous (29) (30).

2.1.7 Spray drying

Spray drying is a method used to convert solutions or suspensions into a powder with one single step. During spray drying, parameters such as temperature and gas flow rate are important for the properties of the desired product. There are several key advantages of spray drying, such as: it is a controllable continuous process, easy to apply on sensitive materials such as peptides, as well as being suitable for different types of solutions. Another advantage is the possibility to control the size of the dried particles (31) (32) (33) (34).

2.1.8 Ex vivo skin model

An ex vivo skin model serves as a representative system for human skin. It is generated from cultivated human skin cells, typically obtained as surgical donations. The model preserves the native extracellular matrix and cellular architecture of human skin, making it well suited for research applications. By expanding these cells in culture, multiple skin models can be produced from the same donor material, conserving both cost and resources (35) (36) (37). The skin model used in this study was cultivated at Chalmers University.

2.2 Techniques

2.2.1 Scanning electron microscopy

Scanning electron microscopy (SEM) is an imaging technique developed in the 1930s. In 1965 a breakthrough came with the discovery of using SEM for visualizing the topography of a surface to obtain information. The modern SEM can detect backscattered electrons and secondary electrons and uses this information to generate an image. Before going into detail about how these types of electrons are used to create an image it is important to discuss how the SEM is structured and what the different components are (38).

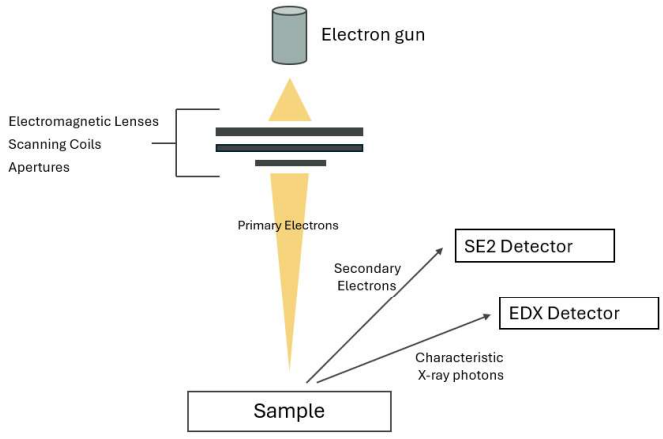

Figure 1: Schematic illustration of the scanning electron microscope

In the upper part of the microscope the electron source is found, from which a beam of electrons is emitted. Primary electrons are sputtered out at a high voltage, creating an electron beam which travels through the SEM until it hits the surface of interest. It is therefore a key

component of the SEM. Another important part of the SEM is the lens assembly. There are different types of lenses used in SEM, which are used to shape and focus the electron beam. Once the beam of electrons passes through the lens, both a magnetic and electric field are generated which applies a force to the electrons making them go in a pathway down the center of the lens causing it to focus. (38).

Another important component in SEM is the specimen, which is the sample in question. The electrons sputtered out from the source go through the different lenses before hitting the specimen. Once the primary electrons have hit the specimen, they will be subject to different kinds of processes resulting in electrons being scattered around in the instrument. The specimen can be of different composition and have different surface topography which will affect how these primary electrons scatter (38).

One type of electrons, which are measured from the specimen are the backscattered electrons. These electrons will undergo multiple scattering events until they emerge from the sample surface, hence the name backscattering electrons. The amount of these backscattered electrons will depend on the weight of the sample atoms; heavier elements tend to increase backscattering of electrons. The backscattered electrons from each scanned point on the image area are detected and generate a current which gets converted into a high-resolution image. The backscattered electrons are used to produce an image showing the average atomic number and some topographical contrast in the analyzed area of the sample (39) (40).

Secondary electrons are those that are formed when loosely bound valence electrons are ejected due to energy transferring interactions. Characteristics for these electrons are the low energies which lead to a short distance of travel. This makes them important for information about surface features and topography and therefore in the imaging of the surface morphology (38) (40) (41).

To achieve high-resolution imaging in SEM several operating parameters must be considered and optimized, for example working distance and aperture size. The image quality is limited by lens aberrations, imperfections of the electromagnetic lenses. Different aberrations, such as spherical and chromatic aberration, degrade the beam focus, limiting the achievable image resolution. Aberrations can be minimized by optimization of the instrument parameters. Another important parameter to optimize is the acceleration voltage, which is the energy of the electron beam. The beam energy influences material interactions and affects image quality and clarity. A higher accelerating voltage tends to enhance SEM resolution because greater beam energy corresponds to a shorter effective electron wavelength, allowing finer features to be distinguished. The relationship is not purely monotonic, though: increasing voltage also enlarges the electron interaction volume within the specimen, which can reduce sharpness. Higher voltage commonly improves the signal-to-noise ratio (S/N), benefiting overall image quality, but it can promote surface charging and increase the risk of beam induced damage on the sample. In contrast, using a lower accelerating voltage improves surface sensitivity by concentrating signal generation closer to surface, commonly used for

non-conductive materials due to mitigating charging and reducing beam damage, though often at the expense of (S/N) and apparent resolution (42) (43) (44).

Material interaction with the electrons can also depend on the spot size of the electron beam on the specimen. This can also influence the results obtained from SEM. In general, the material interaction between the electrons and specimens has the largest influence and will depend on parameters such as acceleration voltage, beam current, spot size among others (38) (45).

There are different modes which can be used on SEM, one being the variable pressure mode. This mode is useful for achieving high resolution images from challenging samples (46). In variable pressure SEM, a small amount of gas is added to the chamber. The gas gets ionized by collisions with the electrons emitted from the specimen and helps neutralize built-up charge on the sample, which reduces charging problems and can increase the signal via a process known as cascade amplification (47) (48).

2.2.2 Energy dispersive X-ray spectroscopy

Energy dispersive X-ray spectroscopy (EDX; also EDS) is a technique used to study the different elements in a sample. An EDX detector system is often mounted onto the SEM to get a combined analysis. During analysis the SEM's electron beam interacts with the sample and knocks out inner-shell electrons from atoms in the material, creating vacancies. When electrons from a higher-energy level fall into the vacancies, X-ray photons are emitted with characteristic energies that are specific to each element. The EDX detector measures these characteristic X-rays to determine the sample's elemental composition (49) (50).

An EDX detector can then simultaneously display all energy X-rays in a spectrum, containing both semi-qualitative and semiquantitative information. In the spectrum there will be different peaks representing different elements. The identification of these elements is performed by the analysis software for EDX (49).

Similarly to SEM, acceleration voltage also influences the EDX outputs. The voltage desired will depend on the sample. Organic materials, e.g. biological samples, typically require a low acceleration voltage compared to many inorganic materials due to a higher sensitivity to radiation damage from the electron beam. However, when it comes to adding the EDX, a minimum acceleration voltage is needed to produce the characteristic X-rays from deexcitation. Moreover, the higher the acceleration voltage, the higher the statistical likelihood of producing the characteristic X-rays from the specimen (42) (51) (52).

The range of energies in the spectrum is measured in keV, and the selected energy range should match the SEM accelerating voltage. Samples with heavier elements often require higher accelerating voltages to excite their characteristic peaks, so a wider energy range may be needed. To ensure all relevant elements are captured, different kV settings and

corresponding keV ranges need to be evaluated. As a rule of thumb, aim for an overvoltage ratio of at least 2 relative to the excitation energy of the lines you want to measure (42) (53).

Accurate elemental identification in a specimen requires EDX energy calibration. Calibration aligns measured peak positions to their true energies based on the detector's resolution, helping minimize peak overlaps. It should be performed using a single element whose calibration peak is isolated (no overlaps within about 100 eV) (42). For light elements, peak positions can shift from their ideal values due to instrumental effects, such as X-ray photon absorption at the silicon entrance window of the detector, creating a risk of interference from nearby energy peaks of other elements. These factors make careful EDX calibration essential (54).

Working distance is the distance between the objective lens and the beam's focus on the specimen. Adjusting working distance changes the objective-lens excitation and therefore the imaging and microanalysis geometry. It affects both SEM image formation and EDX measurements: shorter working distances typically improve lateral resolution and increase the detector's effective angle (enhancing X-ray collection efficiency) (54).

Combining SEM with EDX yields both morphological and elemental information from the same area. SEM-EDX can be acquired on individual particles or across a larger field of view depending on the purpose of the analysis. Together, the methods provide complementary insight: SEM gives morphology and surface features, while EDX provides elemental composition. This combination can quickly deliver information on size, shape, surface topology, and composition, making it a powerful workflow (54) (55).

2.2.3 Sputter Coater

Certain samples, e.g. many organic materials, are challenging to image due to being easily charged, meaning that the electrons accumulate and create "white regions" compromising the image. The charging effect is due to the lack of conductivity of the sample, as the charge induced by the electron beam cannot be easily dissipated from the imaged area. This arises when the primary electrons have hit the surface and induced the accumulation of charge on a nonconductive sample (7) (56) (57).

A common solution is sputter coating the sample with a thin, conductive film before SEM-EDX. The coating provides an electrical path that dissipates charge, improves thermal conduction, and enhances secondary-electron emission, yielding clearer images and reducing beam-induced damage. Sputter coaters deposit uniform films by controlling deposition rate and time (often with sample rotation); thickness is tailored to the sample and coating material (58) (59).

Coatings must be thin enough to preserve surface topography and to minimize their contribution to the EDX signal. If the film is too thick, it can block X-rays from the specimen

and obscure elemental information (54). Carbon is often preferred for SEM-EDX because it contributes little interference to most analyses (42).

Common conductive coatings include gold, platinum, chromium, and gold/palladium (7) (42) (58). Gold offers high conductivity and chemical stability but has larger grain size, favoring low-to-medium magnifications, while platinum has finer grains for higher magnification but can be prone to stress cracking in oxygen (56) (60). Chromium can form very thin, even films with reduced backscattered electron emission but typically requires high vacuum to avoid oxidation (58). A gold–palladium coating is another option, adding palladium keeps the gold grains small making the coating smoother and preserves fine surface details. The trade-off is that both gold and palladium will appear in the EDX spectrum, which can complicate analysis (58) (60).

Typical thickness guidelines depend on the goal and instrument: for high resolution SEM imaging with Pt, Cr, or Au/Pd, films around 2–4 nm are often preferred, whereas for EDX on Oxford systems, about 5–30 nm may be acceptable. In all cases, aim for the thinnest coating that controls charging without compromising imaging or elemental analysis, and adjust for the specific coater and material (42) (54).

2.2.4 Time of Flight – Secondary Ions Mass Spectrometry

Another important technique in imaging analysis is time-of-flight secondary ion mass spectrometry (ToF-SIMS). It works by subjecting the sample surface to a pulsed focused primary ion beam (FIB), which causes sputtering and the emission of secondary ions from the outermost surface layers, with a typical analytical depth of up to approximately 5 nm. A strong electric field generated by the high-voltage extractor rapidly pulls the ions from the surface and accelerates them, while ion lenses focus them into the time-of-flight analyzer. The analyzer separates ions according to their mass-to-charge ratio based on the time they take to travel through it, producing a mass spectrum of molecules and fragments originating from the surface (61) (62).

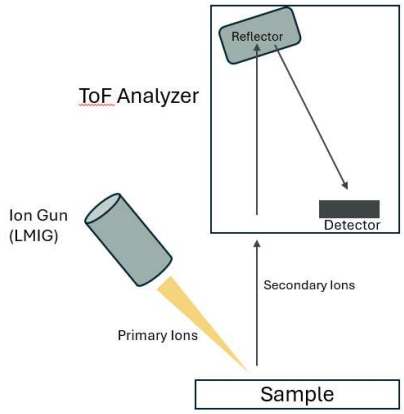

Figure 2: Schematic illustration of the components included in ToF-SIMS

There are four operating modes for ToF-SMIS: spectrometry, surface imaging, depth profiling and 3D imaging (61). *Spectrometry mode* is used to acquire high mass-resolution spectra, for example to identify molecular and fragment ions, but this typically comes at the expense of spatial resolution (~2 µm beam spot for the AstraZeneca instrument using LMIG Bi_3^+ primary ions). When operating in *imaging mode*, chemical images are generated by mapping the spatial distribution of selected ions, achieving nanoscale localization (on the order of ~100 nm). *Depth profiling* consists in repeated cycles alternating sputtering and analysis, typically performed with two different primary ion guns, and is used to reveal chemical composition as a function of depth, providing layer-by-layer information within the sample. (61) (63) (64). Combining 2D imaging and depth profiling, it is possible to achieve *3D imaging* of small regions (65). The ToF-analyzer also allows to record all ions from each pulse in parallel across a broad m/z range, enabling fast acquisition with high mass resolution, and sensitivity to low-intensity signals (66).

Ultra-high vacuum is required for ToF-SIMS to work (67). The samples being analyzed must withstand being subjected to high vacuum levels. The instrument's best operating range is between 10^{-10} to lower 10^{-8} mbar. Operating at these low pressures minimizes gas-phase collisions that would scatter or neutralize secondary ions, preserves surface cleanliness by preventing contamination during analysis, and stabilizes primary-beam/sputter conditions. The range of pressure is important to take into consideration, especially when using biological samples due to the possibility of degradation in vacuum (68).

The choice of the operating mode and the settings optimization is performed based on the desired outcome of the analysis and on the sample's characteristics. For example, the mass resolution in ToF-SIMS is dependent on the pulse length of the secondary ions, which in turn is dependent on the primary beam (62). A high mass resolution using spectrometry mode comes at the cost of significantly decreasing the spatial resolution. If high spatial resolution is needed, then an operating mode with smaller spot size is required. Generally using a smaller spot size leads to local charging, but it can also help to minimize contributions from uneven areas when analyzing samples with high surface topography. The chosen spot size also influences the number of pixels and pixel dimensions for the final image-data, and therefore analysis time and total ion dose (68).

ToF-SIMS offers advantages such as being label free, high throughput and near non-destructive analysis. It is useful for mass spectrometry imaging on rough or otherwise challenging surfaces (69). ToF-SIMS analysis of biological material is challenging due to the presence of a biological matrix with many components, with increased possibility of peak overlapping, but many studies have demonstrated its use on biologically derived samples (5) (70). A key limitation is extensive fragmentation of molecular ions, which reduces molecular information. Methods have been developed to mitigate this limitation and increase molecular signal (71).

SIMS can also give information about the chemical structure of a component since SIMS can produce both molecular and fragmented ions. It is from the fragmented ions and their pattern that one can use SIMS to determine the structure of a compound. Multivariate data analysis can be used to determine the presence and amounts of chemical compounds from ToF-SIMS analyzed samples (67).

2.2.5 M6 Hybrid SIMS (OrbiSIMS)

To overcome the mass resolving power limitations of conventional time-of-flight (ToF) analyzers, an Orbitrap mass analyzer can be used. Orbitrap analyzers can provide substantially higher mass resolving power than ToF analyzers, as well as sub-ppm mass accuracy. This performance is largely due to the detection of ion oscillations frequencies over relatively long transient acquisition times. The transient is the raw time-domain signal recorded by the instrument, from which the ion oscillation frequencies are determined (72).

In Orbitrap-SIMS, the detector and analyzer are different from ToF-SIMS. Ions first enter the C-trap, where they are accumulated and then released in short pulses into the Orbitrap analyzer. The ions are injected into the Orbitrap's electrostatic field between an inner and an outer electrode. Inside this field, the ions orbit the central electrode while oscillating along the axial direction. These axial oscillations induce a small "image current" on the detection electrodes. The detected image current is then processed using fast Fourier transform and then converted into a m/z spectrum (72) (73) (74).

2.2.6 PMA

As part of the sample preparation for SIMS analysis, poly(methyl acrylate) (PMA) is used. PMA is a flexible polymer used as a "sticky surface" for fixing in place powders on a substrate (75). It has a linear formula $(C_4H_6O_2)_n$ and a density of 1.22 g/mL (76). At room temperature PMA appears as a transparent-to-white rubbery material. PMA exhibits moderate hydrophobicity and the physicochemical properties are determined by the side chains. Important properties of PMA are its high flexibility and low water vapor (75) (77).

2.2.7 ImageJ

Fiji is the open-source, plugin-rich distribution of ImageJ focused on biological image analysis. It supports many file formats and handles 2D, 3D, time-lapse, and multichannel data. It is widely used for tasks such as measuring intensities and areas, and for segmentation. A central step in segmentation is thresholding, where manual or automatic methods are applied to separate foreground objects from background and to distinguish different components (78).

3. Method

Before commencing laboratory work, relevant risk assessments must be reviewed and understood for all techniques and specific sample preparation steps. These assessments include safety, health and environment (SHE) requirements and controls for the chemicals and methods employed. Adhering to these measures is essential to protect the laboratory operator and to minimize risk to other personnel in the area.

3.1 Sample preparation

3.1.1 PMA stock solutions

Polymethacrylate (PMA) is supplied to AstraZeneca as a solution in toluene and requires further preparation before usage on samples. The PMA is diluted with toluene to achieve the desired concentration ratio prior to application. The preparation of the different PMA solutions was conducted in a fume hood for safety reasons.

SOLUTION	DILUTION (PMA: TOLUENE)
A	1:3
B	1:6
C	1:9
D	1:12
E	1:15

Table 1: Overview of PMA dilutions setups

Five dilution levels were prepared to produce a range of PMA film thicknesses, shown in Table 1. The PMA thickness decreases from A to E. Each solution was made in a separate vial at the specified ratio and sonicated in an ultrasonic bath for 2–5 minutes to ensure homogeneous mixing. Before usage the sample should be stored for at least 12 h for better results of the PMA distribution.

3.1.2 Sample preparation for samples used for evaluating SEM and ToF-SIMS parameters

Aluminum substrates were prepared and cleaned prior to PMA coating. In a fume hood, substrates were sonicated with heptane (~2 min), transferred, washed with methanol, sonicated, and dried on aluminum foil. To ensure cleanliness and prevent contamination of the aluminum substrate, tweezers and work areas were wiped with ethanol before handling. Each dry substrate was then placed in a foil-lined container. This procedure was applied to all aluminum substrates in the study.

The first samples to be prepared for the evaluation of the different parameters within the instruments was an excipient blend, containing 4 different excipients (with a particle size of 10-100µm), the procedure for this blend can be found in Appendix A1. For these samples, using a Pasteur pipette, one drop of each PMA:toluene solution was dropped onto the corresponding substrates, yielding two substrates per solution (e.g., 2 × Solution A, 2 × Solution B, and so on.). On five substrates, one from each PMA dilution, the excipient blend

was applied. An equivalent amount of blend was added to each, followed by gentle vibration/tapping to promote adhesion and removal of excess powder by inversion. This procedure yields ten substrates: five coated only with PMA solutions and five coated with PMA including the excipient blend, shown in Figure 3. Substrates carrying the powder blend are labelled AP-EP (P indicates the presence of the excipient blend). All substrates were stored in a closed container until analysis.

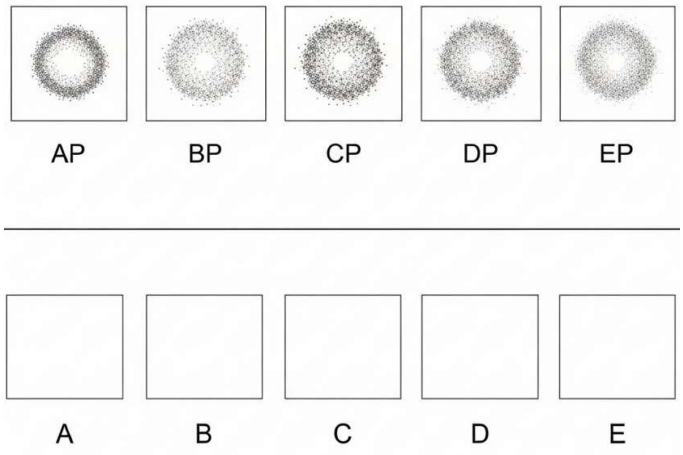

Figure 3: Samples used to evaluate PMA thickness; image generated by AI.

This procedure was similarly used for another type of sample, spray-dried powder (1-10µm), with the difference that this step was conducted in a laminar flow safety cabinet because of the higher occupational exposure concern associated with the powder. For these samples only PMA:toluene solution A, C and E were used and added onto the aluminum substrates along with the spray-dried powder.

For both the excipient blend and the spray-dried powder, a common SEM sample was prepared by applying carbon tape to the SEM stub and adhering the powder onto the tape. These samples served as references for assessing the influence of PMA in SEM-EDX.

3.1.3 Sample preparation for optimization of tilting angles within SEM-EDX

Two samples with larger lactose particles (150-250µm) were prepared to assess imaging angles across both techniques, as larger particles facilitate visualization of structural features and help identify the optimized angle. Both samples used the thinnest PMA layer (thickness E). A small number of particles were placed onto the PMA and gently pressed to adhere. Because particle count was intentionally low, the usual step of vibrating to remove excess powder was not performed to retain the deposited particles.

3.2 Method optimization of SEM-EDX

The preselected settings on EDX can be summarized in Table 2, which were used for the SEM-EDX analysis as starting points and the Image resolution had to be altered due to charging, those cases are noted and explained within relevant sections.

Image resolution	512x512 pixels
Pixel Dwell time	100 µs
Process time	4
Number of Channels	1024

Table 2: Starting parameters for EDX acquisition.

3.2.1 Acceleration voltage

To evaluate the influence of acceleration voltage on SEM imaging and EDX, a systematic analysis was conducted. From the samples prepared in Section 3.1.2, sample CP was selected. At each voltage, imaging and elemental analysis were completed before increasing the voltage in 1 kV steps (2 kV, 3 kV, etc.) until charging artifacts appeared in either the SEM image or the EDX signal, at which point testing stopped. The same workflow was applied to excipients without PMA and to the aluminum substrate. Image locations were varied between voltages to reduce the risk of localized charging. To quantify the influence of acceleration voltage on SEM images, ImageJ was used to measure the pixels and then calculate the percentage of pixels being charged, selecting a threshold value seen in Table 3 for the measurements during all images. From the measured pixels lying within the threshold the percentage of the overall image was calculated using equations presented in Appendix A2 and A3.

Upper threshold	255
Lower threshold	150

Table 3: Thresholds used to quantify pixels exhibiting charging effects.

To measure the influence of acceleration voltage on EDX analysis, the same starting settings found in Table 2 were used for all EDX runs. The image resolution did change for the higher acceleration voltages (4 kV for the middle thickness (CP) and 6 kV for the typical SEM sample), the change was from 512x512 pixels to 256x256.

Acceleration voltage was also evaluated for the spray-dried powder. Ideally, the same assessment as for the excipient blend would enable direct comparison. Because PMA increases charging risk, the initial setup used spray-dried powder on carbon tape without PMA to reduce charging while configuring the SEM. However, charging occurred during stage elevation at 2 kV. The voltage was therefore reduced to 1 kV to stabilize the image and set the working distance. Since 1 kV is insufficient for EDX, the voltage was then raised to 2 kV, which again induced charging and particle movement, posing a risk to the instrument.

3.2.2 Variable pressure mode

After assessing the impact of acceleration voltage and recognizing the need to reach higher kV without inducing charging, the next step was therefore to assess variable pressure (VP) mode. This step is critical for establishing a workable method to analyze PMA and aluminum substrates used for ToF-SIMS with the SEM-EDX, as PMA showed to increase the likelihood of charging. To evaluate VP mode, sample CP was used to test increasing acceleration voltages and the feasibility of reaching higher values. The workflow proceeded until charging artifacts appeared in either the SEM images or the EDX signal. Given VP's reduced resolution and signal-to-noise ratio, testing began at 10 kV with a chamber pressure of 20 Pa.

The variable pressure mode was also evaluated for the spray-dried powder due to showing a different response to the acceleration voltages than the excipient blend. To mitigate charging, testing began at 5 kV and increased incrementally until charging was observed; analysis was feasible up to 8 kV. Within this range, both imaging and elemental detection were performed. Because of the high charging risk, only samples without PMA were used.

3.2.3 Working distance

When using VP mode, the image resolution and S/N deteriorated compared to the standard method due to scattering of the electron beam by the gas molecules in the sample chamber. This produces an electron "skirt" around the probe and reduces the S/N ratio, an effect that likely worsens with increasing working distance (WD). During EDX installation the WD was set to 8.5 mm by default and to improve imaging, the WD was later reduced to 5.0 mm. To enable a direct comparison, a cluster on sample AP was located so the same site could be analyzed at identical acceleration voltages for both WD. This evaluation was limited to the excipient blend to minimize charging risk.

3.2.4 PMA thickness

The recommended PMA film thickness for ToF-SIMS analysis has been established at AstraZeneca. To enable a correlative workflow, samples must be optimized for both techniques; therefore, the effect of PMA thickness needs to be evaluated by SEM. The different PMA thicknesses (AP-EP) were analyzed by SEM-EDX under identical parameters to determine how film thickness affects elemental detection. For the EDX evaluation, regions near the center of each sample were measured, and an acceleration voltage of 3 kV was used for all samples.

To evaluate the effect of PMA thickness on SEM image quality, three locations per each PMA thickness were examined at each accelerating voltage. For each measurement, the scan was stabilized by maintaining a constant scan rate for 30 seconds prior to image acquisition. Images were then acquired using identical parameters for scan speed and line averaging to ensure comparability across conditions. The measurement sequence at each location proceeded as described in Table 4.

	Scan speed	Linear average	Time
Sputtering on the sample	4	N = 1	30 sec
Image generation	7	N = 11	55,6 sec

Table 4: Protocol for achieving comparable image quality across all PMA thicknesses.

Each image was processed in ImageJ to quantify charging by applying a consistent intensity threshold, presented in Table 5. Because the field of view included the SEM settings bar, the initial pixel counts encompassed this overlay. Accordingly, the measured values were corrected by subtracting the pixel contribution of the SEM settings bar, based on its known pixel area. The detailed calculations and the quantification equation are provided in Appendix A2, A3 and A4.

Upper threshold	255
Lower threshold	200

Table 5: Selected threshold for counting pixels exhibiting charging artifacts.

The thickness of the different PMAs was measured by sectioning the excipient samples through the center and removing half of it, leaving a cross-sectional edge that exposed the substrate, the PMA, and the excipients. Using the built-in SEM measurement tool, the PMA thickness was measured, an example of this can be seen in Figure 4. For each PMA, 5-6 locations were analyzed, and the mean thickness was calculated.

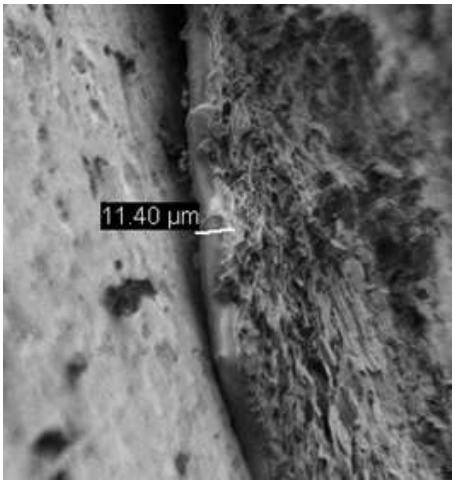

Figure 4: Illustration of the SEM method used to measure PMA thickness.

3.3 ToF-SIMS methodology

Due to ToF-SIMS being a more complex instrument than SEM-EDX, and because an established workflow already exists at AstraZeneca, the method optimization was focused on SEM-EDX, but comparisons between the two techniques were made.

3.3.1 Setting up the instrument

In the ToF-SIMS at AstraZeneca, the back mounted sample holder can hold up to 18 samples during each analysis. The substrates commonly used are the aluminum substrates which have been previously described within the sample preparation Section 3.1.2. A standard PMA thickness has been established and used routinely; however, the full range of PMA thicknesses still needs to be evaluated by ToF-SIMS.

Imaging mode was selected for the analysis of the samples with the ToF-SIMS. Depending on the sample and interest, different positions and number of areas can be analyzed for each specific sample. The height and X-Y coordinates for each analysis area were identified and saved in a "position list" file, then loaded into a recipe for automated data collection. The SIMS images were collected over a 100 μm × 100 μm area for each saved position for the spray-dried powder sample and excipient blends.

A limitation is that, to avoid sample damage, focus was optimized only on the standard grid rather than on each individual sample. Combined with the automated workflow (which implies that the stage needs to drive to saved locations before each acquisition and can therefore introduce positioning / focus errors due to stage movement tolerances) this may result in some images not being captured at the highest achievable resolution.

3.3.2 PMA thicknesses

To assess whether PMA thickness affects ToF-SIMS, analogous to the SEM-EDX evaluation, all PMA thicknesses were systematically tested. For each thickness containing excipients, six locations were measured per sample. At each location, an ion image and a m/z spectrum were acquired in both positive and negative polarity. The analysis was run overnight to cover all five samples. This yielded two images and two spectra per location, totaling 12 images and 12 spectra per PMA thickness for evaluation.

3.3.3 Composition analysis of excipient blend and spray-dried powder

ToF-SIMS produces full spectra and images of detected compounds for each selected location. Before handling the data, the spectrum requires calibration to ensure reliable, reproducible assignments and minimize mass errors. After calibration, a mass-interval list (peaks of interest for hyperspectral image processing) was generated. For the excipient blend, AstraZeneca's established characteristic peaks for each excipient helped with software familiarization. Although the software can preassign (with compound formula) peaks based on deviation and likelihood, these assignments require verification. Characteristic peaks were chosen by comparing spectra of individual references and selecting high-intensity, compound-specific signals, then creating a mass-interval list applicable to all images. For the spray-dried powder, peak characterization was developed de novo without predefined features; peaks exhibiting distinctive spatial distributions were added manually.

3.3.4 ImagePipeline

ImagePipeline is a software developed in-house at AstraZeneca by Mats Josefson. The program deconvolutes the ToF-SIMS hyperspectral image data performing MVA and generating MVA component-images, each assigned to a reference compound present in the formulation. First, a model is built by training on reference materials, reference images and their associated spectra. During training, the model learns to recognize the mass spectrum characteristic for each compound, then the model is used to predict and match the spectra of each generated MVA component to the correct reference spectrum. For instance, in this study, each excipient is provided as a separate reference. By supplying a representative image and a mass spectrum for each excipient, *ImagePipeline* can distinguish excipient particles from the background (PMA) and differentiate among the excipient classes. Once the model is created, all ToF-SIMS images containing excipients can be processed, and the spectral information for each pixel will be deconvoluted and matched to the spectra of the reference excipients or PMA.

ImagePipeline also allows to automatically generate RGB colour-overlay images for each prediction, where the distribution of three components can be visualized. For the 5-component samples (4 Excipients + Background (PMA)), two different RGB colour-overlay images were made.

3.4 Image location and Registration

3.4.1 Creating markings for finding the same image location

After optimizing the key parameters for each technique, the next step in a correlative workflow is to analyze the same region on both instruments. This requires a reliable method to mark the target area. Based on previous learnings, it is recommended to begin with ToF-SIMS because SEM-EDX is more destructive. ToF-SIMS can also generate craters with the ion beam, which provide durable, high-contrast markers that simplify relocation of the site and improve the consistency of correlative measurements. This capability is another reason why starting with ToF-SIMS is the most effective way to establish the correlative workflow.

To mark the area of interest and reliably relocate the same site on both instruments, a fiducial mark and a defined orientation were required. Maintaining a consistent orientation is essential to analyze each location in the same way it was acquired in ToF-SIMS. The initial approach used ToF-SIMS to fabricate markers by sputtering with the “long pulses” setting, producing small craters that penetrated the PMA layer and cleared the area from the sample. Three fiducial craters were arranged in an L-shaped pattern, the distances between each image and the marker were selected within the ToF-SIMS instrument creating the scheme seen in Figure 5. The combination of known distances and the ToF-SIMS image field-of-view dimensions provide a practical guide for relocating the same regions with SEM-EDX. In Figure 5 the blue squares symbolize the craters while the white squares are the areas being analyzed with both ToF-SIMS and SEM-EDX. The distances noted in Figure 5 were adjusted during the process, depending on the sample type.

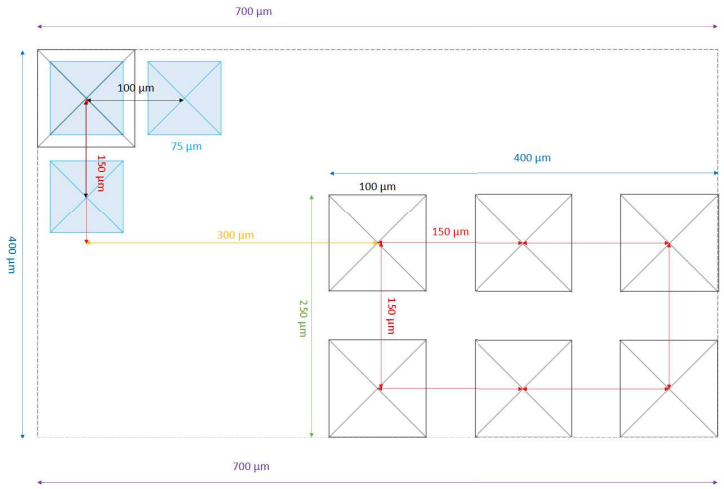

Figure 5: Schematic of image locations relative to the added fiducial craters.

The first samples for testing the use of fiducial craters were performed on samples AP, CP and EP, covering the whole range of PMA thicknesses developed. Within the SEM software, measurement tools were used to determine the distances from each analysis location to the fiducial craters and to neighboring locations. Each SEM site was then compared with the corresponding ToF-SIMS image to confirm that the SEM field of view encompassed the intended region.

3.4.2 Optimization of angles within the instrument

During image localization and registration of the same regions in samples AP, EP, and CP, visual assessment indicated that the two instruments produce images from different viewing angles. In ToF-SIMS, the ion beam angle is approximately known (nominally 45° per the IONTOF manual). In contrast, the electron beam in SEM is perpendicular to the sample surface, while the SE2 detector is positioned at an angle relative to the beam. Consequently, selecting an appropriate stage tilt and rotation for the SEM stub is an important step for cross-instrument data alignment and image registration. First, different stage rotations and tilts were evaluated in the SEM to identify the best tilt position, which is presented in Appendix A5. The working stage rotation was set to 285°, with a scan (sweep) rotation of 265°. However, the scan rotation can be adjusted to match the image as perfectly as possible to the ToF-SIMS image.

To evaluate the angle range, two sample types containing larger lactose particles (prepared as described in Section 3.1.3) were used. After acquiring ToF-SIMS images for both sample types, the next step was to evaluate how tilting would impact the SEM image. For each ToF-SIMS image location on both sample types, SEM stage tilt was systematically varied from 0° to 45° in 5° increments. Tilting the stage changes the electron beam's angle of approach to the sample. The working hypothesis was that a 45° tilt would best mimic the ToF-SIMS ion beam angle, since ToF-SIMS operates at approximately 45°.

After imaging across the full tilt range for all image locations on the two samples, the recommended tilt was determined by quantitative image registration. A computer modelling program was developed in-house at AstraZeneca by Gabriele Colcerasa , with the aim to overlay each SEM image with its corresponding ToF-SIMS image and optimize the fit. This was done for all angles generated within the SEM and from this the model gave the best angle range to be 35º – 40º. The angle range (35°– 45° tested) and the previous determined rotation were evaluated for EDX. The EDX results were consistent with those from SEM imaging, likely because the outcome is primarily governed by how the electron beam strikes the specimen rather than by the detector positions.

3.4.3 Image registration

Image registration was performed to align and overlay the images and corresponding chemical maps generated by ToF-SIMS and SEM-EDX. The aim was to combine the high-resolution structural information from SEM with the chemically resolved information from ToF-SIMS and EDX into a single interpretable representation.

To achieve this, a custom end-to-end computational workflow was developed in Python, called Mireg for multi-modal image registration. The program consists of a series of scripts that sequentially handle data import, preprocessing, image registration, transformation of signal maps into a common coordinate system, region classification, and final visualisation. The workflow uses the SEM electron image as the base reference frame. The ToF-SIMS total ion image is first aligned to the SEM image to account for differences in magnification, rotation, translation, and field of view as seen in Figure 6.

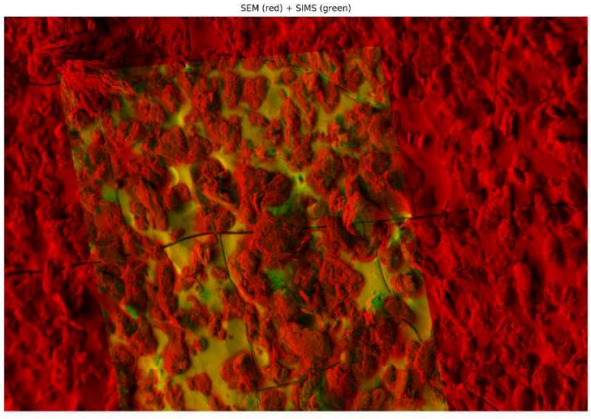

Figure 6: Image Registration SEM + SIMS

In parallel, the electron image associated with the EDX acquisition is independently aligned to the SEM image (see Figure 7), and the resulting transformation is then applied to all associated EDX elemental maps. In this way, both the ToF-SIMS and EDX datasets are brought into a common SEM coordinate space.

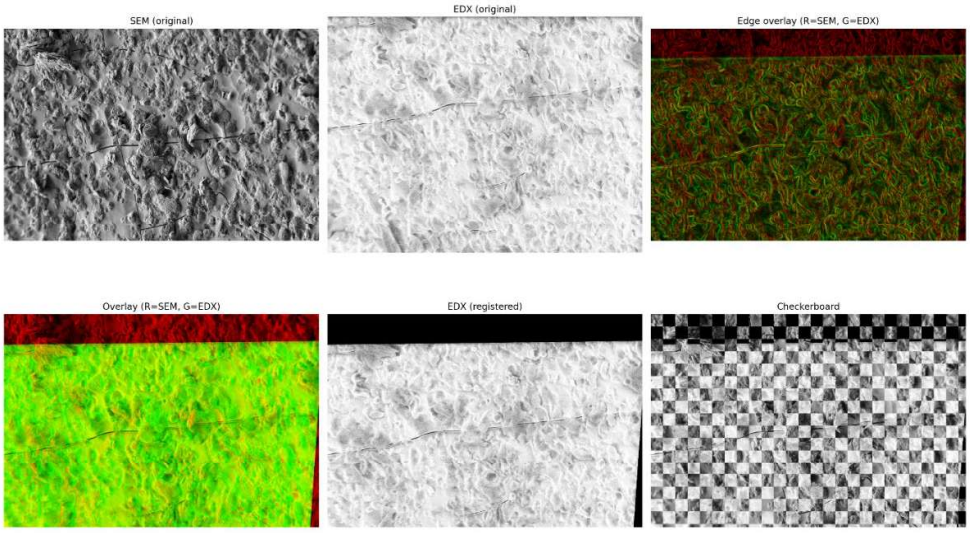

Figure 7: Image registration of EDX electron image onto SEM coordinates

The ToF-SIMS data are further processed using ImagePipeline, which generates principal component masks representing chemically distinct regions within the dataset. These SIMS-derived masks are then registered into SEM coordinates and used as spatial classes for downstream interpretation of the EDX data. The program subsequently calculates where each EDX elemental map intersects with each SIMS component, allowing the elemental signal to be assigned to different chemically defined regions.

The registration process leverages the use of manual landmark selection. The program determines the recommended alignment by comparing image features across modalities, using edge-based information, mutual information metrics, and optimisation over scale, rotation, and translation. This enables reproducible alignment between datasets acquired using different detectors and imaging principles.

The final output of the workflow is a composite summary figure that integrates morphology and chemistry into a single view. The top row shows the raw SEM electron image, the SEM image with the SIMS principal component segmentation overlaid, and the SEM image with all EDX elemental maps overlaid simultaneously. The lower panels display each individual element separately, showing only the regions where the EDX signal intersects with a given SIMS component. This enables direct identification of whether an element is preferentially associated with one region or another or distributed across both. In addition, quantitative metrics are generated for each element, including total coverage and relative signal density across the different SIMS-defined regions.

This end-to-end workflow therefore provides a structured and automated route from raw multimodal images to a final correlative output, enabling direct comparison between morphology, ToF-SIMS-derived segmentation, and EDX elemental localisation.

3.5 Applying the correlative workflow

After evaluating both techniques and establishing a correlative workflow, the next step was to apply it to relevant samples. The workflow was implemented on a spray-dried powder containing bovine serum albumin (BSA) and leucine, as well as on the previously studied excipient blend. To test a fundamentally different, non-powder sample type, an ex vivo human skin model exposed to $AlCl_3$ was also analyzed.

3.5.1 Spray-dried powder with protein

Applying the correlative workflow on the spray-dried powder containing Bovine Serum Albumin as the model API, three different concentrations of BSA were used to evaluate the differences between them. For this sample, the workflow also helps to determine the localization of BSA within the components to assess the heterogeneity of the sample which has an important role when it comes to dosing.

Samples were obtained from Uppsala University and included four reference components, along with three mixtures of these components prepared at different concentrations (5,10 & 20%) of the active protein (BSA). For this study, the PMA dilution was 1:15, yielding a coating of approximately 0.5–1.0 µm. Spray-dried material was prepared on the PMA as described in Section 3.1.2. In parallel, individual reference for each component was prepared to serve as standards for building the model within ImagePipeline.

Based on learnings from ToF-SIMS method optimization, fiducial craters were introduced to enable relocation of the same fields of view across instruments. Craters were produced as described in Section 3.4.1, and the distances from each crater to the intended imaging locations were recorded. ToF-SIMS acquisition was then performed first. For each sample and each reference, image data (100µm x 100µm) were collected, and m/z spectra were acquired, calibrated, and processed using a predefined mass-interval list. The reference datasets and their m/z lists were imported into the ImagePipeline to obtain the model. Before applying the model to the three concentration samples, total ion images were exported to support matrix transformation during correlative alignment.

Following ToF-SIMS, samples were transferred to SEM-EDX. To keep conditions as consistent as possible with ToF-SIMS, SEM sample preparation and mounting were carried out in an ultra-dry laboratory. Samples were arranged as specified in Appendix A5. Each sample was tilted between 30° and 45° to optimize EDX collection; for these small particles, 30° was found to work best for the image registration (lower than the angle used for lactose particles). EDX measurements were then acquired at 10 kV with a 30° tilt in variable-pressure mode (30 Pa).

Outputs from both instruments were combined and entered the registration program to compute the required transformation and generate the correlative datasets. The resulting outputs permit visualization of the spatial distribution of each reference-defined component alongside elemental maps, and estimation of how strongly each element correlates with the

reference components. This workflow was applied to each concentration level, enabling comparison across concentrations and assessment of any property changes.

3.5.2 Excipient blend

After optimization, the same excipient blend was analyzed using the correlative workflow. The components of the excipient blend are MgSt, MCC, SSG and DCPA, all containing different characteristic elements. Showing another purpose of the correlative workflow of identifying the different components within a blend to draw conclusions about blending, properties and topography.

The correlative workflow was conducted similarly to the workflow described in section 3.5.1, using the same PMA dilution (1:15) and the same image location (100µm x 100µm) markings. The angles tested for this sample type was 35° – 45° degrees with the best angle being 35° degrees, used for EDX analysis. After generating all outputs from both techniques, the image registration was conducted.

3.5.3 Ex vivo human skin exposed to $AlCl_3$

As an additional sample type, an ex vivo human skin model exposed to $AlCl_3$ in ethanol was used to assess how $AlCl_3$ exposure affects analyte distribution across the tissue. The model (provided by Chalmers University) was cryosectioned at −20°C to 12 µm and mounted on silicon wafers and glass slides for instrumental analysis. Due to time constraints and issues with the top-mounted holder, only the silicon wafer-mounted sections could be analyzed with the bottom-mounted holder; the corresponding control sections on glass were therefore not measured. From the frozen state, sections were dried under ToF-SIMS vacuum, mounted, and three locations per sample were argon-sputtered to remove surface contaminants prior to acquisition. ToF-SIMS images (200 µm × 200 µm) and m/z spectra were then collected at each sputtered site. Fiducial craters were not added in order to avoid potential tissue damage.

4. Results

4.1 Factors in SEM-EDX

Charging is a common issue in SEM and EDX when imaging non-conducting specimens (see Section 2.2.3). It occurs when incident electrons are not conducted away and instead accumulate on the sample surface, creating local electric fields. This charge buildup degrades data quality by causing image drift, uneven or inverted brightness, loss of fine detail, and blurred regions. The accelerating voltage sets the primary-electron energy, at higher kV the beam penetrates deeper, and more electrons enter than escape causing charge accumulation. Operating at lower kV can move the system closer to charge balance and reduce charging artefacts. In practice, each insulating material has an operating window where charge balance is achievable, this window depends on composition, microstructure, thickness, and surface roughness, as well as beam conditions (7) (56) (57). Understanding and tuning parameters such as accelerating voltage are essential to build a robust correlative workflow.

4.1.1 Acceleration voltage

To evaluate the optimal acceleration voltage for SEM-EDX, two specimen types were examined: a representative “middle” PMA-thickness (CP). SEM imaging was conducted before and after EDX for each acceleration voltage. The images acquired before EDX acquisition can be seen in Figure 8, while all images are displayed in Appendix A6, for the acceleration voltages used (2-4 kV).

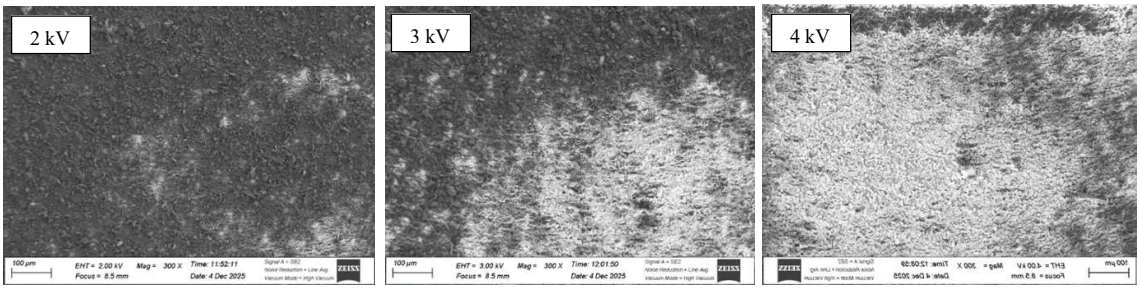

Figure 8: Charging accumulation over different acceleration voltage (2-4 kV)

To achieve quantified results regarding the influence of acceleration voltage, the area percentage of charging in the images was calculated (see Appendix A2 and A3) and summarized in Figure 9 .

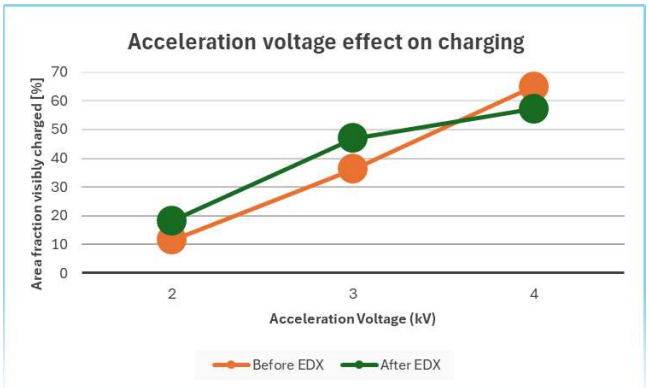

Figure 9: Quantified charging (%) at three acceleration voltages.

Figure 9 together with the visual observation found in Figure 8 and Appendix A6, shows that for increasing acceleration voltages the area percentage of visible charging increases within the SEM images. Since SEM will be coupled with EDX during this study, it is also important to evaluate how the acceleration voltage impacts the EDX analysis.

The acquisition parameters for EDX were kept identical, described in Table 2 for 2-4 kV, while lowering the image resolution to 256x256 pixels for 5 kV due to the increase of charging. The image location and EDX analysis were conducted at the same spot for all acceleration voltages. Comparing the acceleration voltages, Table 6 shows the differences in elemental weight percentages. Even though there is no clear trend in the detected elemental percentages, the standard deviation generally decreases with the increase of acceleration voltage. Another finding from Table 6 is that for higher acceleration voltages, the greater electron penetration depth led to a higher detection of aluminum (from aluminum substrate). Notably, at higher voltage 5 kV, the software resolved the spectral overlap between carbon and calcium, enabling clearer distinction between these elements. This shows the importance of using higher acceleration voltages for making it possible to detect certain heavier elements.

Element	Wt% 2kV	Standard Deviation	Wt% 3kV	Standard Deviation	Wt% 4kV	Standard Deviation	Wt% 5kV	Standard Deviation
Carbon	70.6	6.6	32.9	3.5	69.4	0.3	63.0	0.4
Oxygen	14.9	1.4	10.5	1.1	21.5	0.2	24.8	0.3
Phosphorus	9.8	8.4	0.2	0.2	0.2	0.1	0.2	0.1
Magnesium	3.5	0.5	1.6	0.2	3.2	0.1	3.0	0.1
Aluminum	0.9	0.6	1.0	0.1	4.0	0.1	6.6	0.2
Sodium	0.3	0.2	0.2	0	0.4	0.1	0.3	0.1
Calcium	0	33.2	53.4	5.0	0	26.3	0	0.7
Potassium	0	7.4	0	0	0	4.3	0	0.4
Fluorine	0	0	0.2	0.1	0.6	0.1	0.1	0.1
Nickel	0	0	0	0	0.7	0.1	0.2	0.1

Table 6: EDX elemental weight% detected at different acceleration voltages.

Taken together, the cross-voltage results show that beam energy strongly affects charging artefacts and data quality. Critically, moving to higher accelerating voltages improves EDX performance, delivering clearer peak separation, higher count rates, and lower standard deviations in elemental weight percentage. At the same time, low kV remains preferable for

SEM imaging of insulating samples to preserve surface detail, limit interaction volume, and minimize charging artefacts. Consequently, future measurements should prioritize the highest practicable kV compatible with the specimen's charge tolerance for EDX, while using lower kV for high-fidelity SEM imaging of the same regions to balance analytical precision with surface fidelity.

To assess voltage-dependent behavior across sample types, a second material, a spray-dried powder containing biological components was examined. At 2 kV, visual inspection revealed pronounced charging, far exceeding that of the excipient blend. Using the same exposure, and thresholding as for the excipient sample (Figure 8) the spray-dried powder showed 87% of the imaged area exhibiting visible surface charging as bright regions close to image saturation at 2 kV (Figure 10), compared with 11.5% for the excipient blend at the same voltage. This assessment was completed before EDX acquisition. Because of the high charging level and evidence of particle dislodgement from the surface, no further evaluation of accelerating-voltage effects on SEM imaging or EDX analysis was pursued for this sample due to the risk of damaging the EDX detector window.

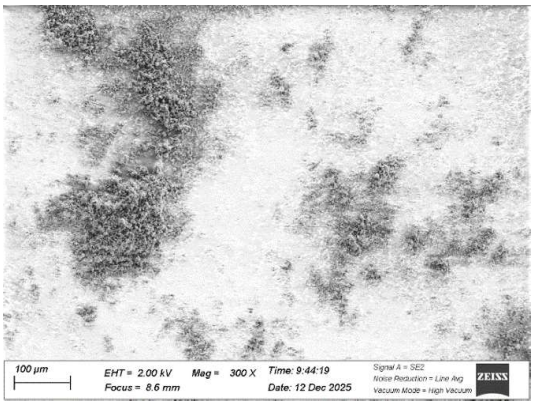

Figure 10: SEM image showing charging at 2 kV in the spray-dried powder.

Comparing the excipient blend (Figure 8) with the spray-dried powder (Figure 10) indicates that SEM–EDX parameters are inherently sample dependent and should be tailored rather than standardized. The spray-dried particles show pronounced charging that degrades image quality and EDX quantification, likely due to their finer particle size and porous, cohesive agglomerate microstructure (79) (80). Figure 10 also suggests that the particle clusters dissipate charge differently, leading to partial suppression of secondary electron emission which causes them to appear less bright. Material-dependent contrast and contrast reversal mechanisms are described in *Principles and Practice of Variable Pressure/Environmental Scanning Electron Microscopy* (38) Implementing charge-aware operating conditions, enables stable imaging and reliable EDX quantification on the same regions. Building these practices into routine methods increases reproducibility, supports comparable results across samples and conditions, and ensures that interpretations reflect true material behavior rather than beam-induced artefacts.

4.1.2 Variable pressure mode

Due to limitations with charging in the standard high vacuum mode a solution for reaching higher acceleration voltages was necessary, which is the reason why variable pressure mode was evaluated. In this comparison, the VP mode is represented by the CP sample at 15 kV, while the high vacuum mode is represented at 5 kV at the same magnification of 400x and the same image location. A side-by-side comparison between the weight percentages can be found in Table 7, while the respective elemental maps are found in Appendix A7 and A8.

	Weight% at 5 kV	**Standard deviation**	**Weight% at 15 kV**	**Standard deviation**
Carbon	63.0	0.4	43.3	0.1
Oxygen	24.8	0.3	32.5	0.1
Phosphorus	0.2	0.1	0.1	0
Magnesium	3.0	0.1	0.7	0.01
Aluminum	6.6	0.2	17.9	0.1
Sodium	0.3	0.1	0.2	0
Calcium	0	0.7	0.1	0
Potassium	0	0.4	0	0
Fluorine	0.1	0.1	1.5	0
Nickel	0.2	0.2	1.8	0.1
Sulfur	0	0	1.9	0

Table 7: Elemental composition in high-vacuum (5 kV) and variable-pressure (10 kV) SEM: a comparison.

Comparing the results in Table 7, shows that with higher kV detection of trace elements from the aluminum substrate such as nickel, sulfur and fluorine can be detected. These elements are detected for both voltages, with a greater amount for the higher acceleration voltage (15 kV) The identification of nickel also provides the result that having a higher acceleration voltage makes it possible to detect heavier elements in the samples. Results in Table 7 also support the previous findings that with a higher acceleration voltage the standard deviations decrease, enhancing the need for high kV.

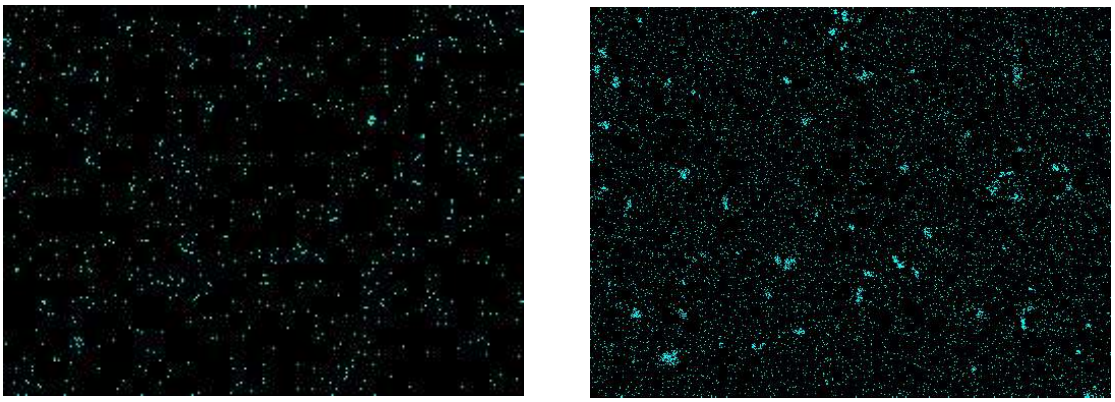

(a): Na elemental map at 5 kV (b): Na elemental map at 15 kV

Figure 11: Elemental maps of sodium (Na) at different vacuum modes and acceleration voltages.

Comparing the elemental maps in Figure 11, Appendix A7 and A8, the higher acceleration voltage yields clearer, less noisy maps due to improved detection efficiency Figure 11 also shows improved localization of particle compositional information, attributable to the higher signal-to-noise ratio at increased kV. Results in VP show that operating in variable-pressure mode enables higher accelerating voltages, which facilitates detection of heavier elements, increases penetration depth, and yields clearer elemental maps.

The VP mode was also tested on the spray dried sample to examine how this type of sample behaved during the higher acceleration voltages. Figure 12a and 12b shows the EDX electron images acquired during analysis at 5 kV and 7 kV, respectively. Increasing the acceleration voltage to 7 kV led to charging, which limited further increases to 8 kV. Appendix A9 summarizes the elemental weight distributions obtained at the different voltages. Variable-pressure mode expanded the usable acceleration voltage range, as illustrated by the spray-dried powder: comparing Figure 10 with Figure 12b, measurements progressed from severe charging at 2 kV in high vacuum to stable EDX acquisition at 7 kV at VP (20 Pa), and even 8 kV for lower-resolution analysis.

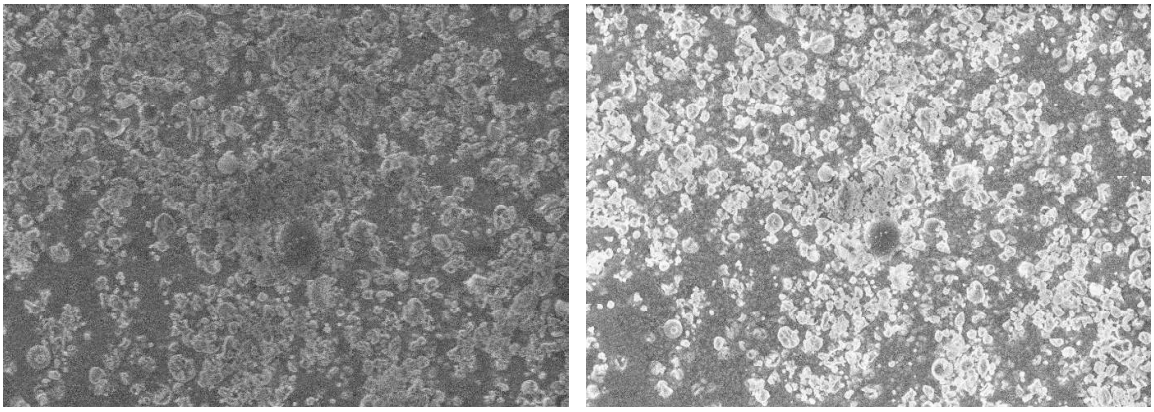

(a): Surface at 5 kV (b): Surface at 7 kV

Figure 12: SEM images of the spray-dried powder across accelerating voltages (VP mode).

4.1.3 Working distance of EDX detector

During the initial experiments, the EDX detector geometry used a default working distance of 8.5 mm. Because variable-pressure (VP) SEM was required to reach higher kV, it was hypothesized that reducing the electron path length in gas could improve beam quality by mitigating scattering and the associated skirting effect. Accordingly, the detector was adjusted to a WD 5.0 mm to assess how working distance under VP conditions influences EDX count rates and mapping resolution. For both working distances an identified cluster on sample AP was used for a comparison. Both EDX analysis were conducted with 512x512 pixels and using the same process time. Other important parameters obtained from the analysis are summarized in Table 8.

WD	Total counts	Live time	Energy range	Number of Channels
5.0 mm	1 018 306	196.6 s	20 keV	2048
8.5 mm	1 136 785	196.6 s	20 keV	2048

Table 8: Different settings for the analysis of how and if working distance influences the EDX analysis.

Table 8 indicates no meaningful differences between the tested settings, aside from a modest increase in total counts at a working distance (WD) of 8.5 mm. The respective elemental composition was obtained to be similar for both working distances, which can be seen in the table presented in Appendix A10.

The EDX maps in Figure 13 compare layered images acquired at the two WDs. With the WD lowered to 5.0 mm, the shadow effect appears reduced: the grey, element-free region seen in Figure 13a shows detectable signal in Figure 13b. However, this difference may also reflect minor changes in stage rotation or sample positioning between acquisitions.

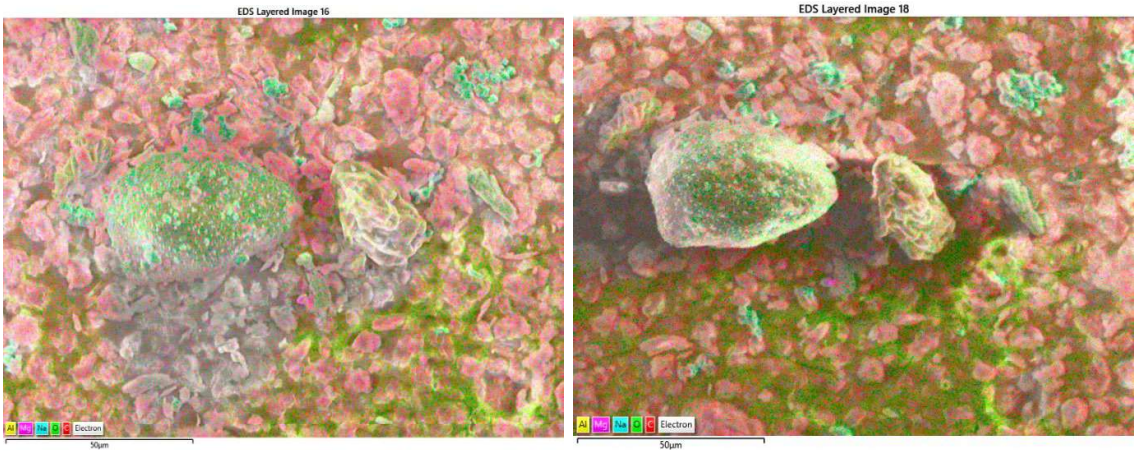

(a) Wd 8.5 mm *(b) Wd 5.0 mm*

Figure 13: Elemental map overlay for sample AP at two working distances.

4.1.6 PMA thickness

PMA thickness sets the gap between the excipients and the conductive aluminum substrate, influencing both elemental detectability and the propensity for sample charging. Because PMA was selected as a substrate based on ToF-SIMS sample preparation requirements, its impact on SEM-EDX must also be assessed.

To assess composition effects, all PMA thicknesses were analyzed at a fixed accelerating voltage of 3 kV with identical EDX acquisition settings. Elemental compositions for the different PMA thicknesses are reported in Appendix A11. At 3 kV, the results indicate a thickness-dependent substrate contribution: for the thick films (A and B) the electron interaction volume does not reach the underlying aluminum, consistent with no Al signal in Appendix A11 and pronounced charging in Figure 14. Whereas for the thinner films (C–E) the interaction volume extends to the substrate, as evidenced by detectable Al in Appendix

A11 and reduced charging in Figure 14, which shows a substantial thickness difference between A and B versus C–E. Together, these observations indicate that samples C–E lie within the penetration range at 3 kV, while A and B do not.

The PMA thickness influenced the charging as well as the maximum reachable acceleration voltage. By visible identification charging can be seen to increase for the thicker thicknesses, this can be seen in Appendix A12. Figure 14 presents the different PMA thicknesses and the area percentage of SEM image that was charged for each acceleration voltage. In the same figure the standard deviation can be seen for each sample mean, at each acceleration voltage due to having technical replicates at each kV. Because each sample includes replicates at each accelerating voltage, the mean of the measurements reported in Appendix A4 is used, and standard deviations are calculated from those values.

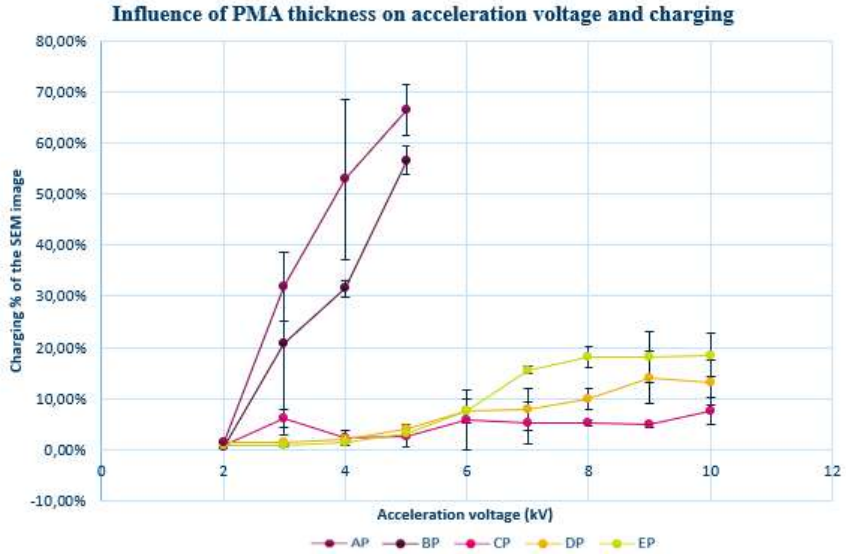

Figure 14: Quantified charging (%) of samples at different accelerating voltages.

Figure 14 indicates that thicker PMA layers (samples A and B) exhibit increased charging, whereas samples C–E show lower charging even at higher accelerating voltages. These supports using thinner PMA films for SEM-EDX to reduce overall charging. Among the thinner sets, a difference emerges at higher kV: sample E displays more charging than samples C and D. Accordingly, a mid-range PMA thickness (sample C) appears preferable for balancing charge control and analytical performance.

PMA thickness	Dilution	Mean thickness	Range of thickness
A	1:3	10.57 µm	8.0 – 11.4µm
B	1:6	3.88 µm	2.0 – 5.0 µm
C	1:9	1.84 µm	0.9 – 3.0 µm
D	1:12	1.18 µm	0.8 – 1.5 µm
E	1:15	0.63 µm	0.45 – 1.0 µm

Table 9: Summary of mean thickness and ranges for PMA solution.

Table 9 reports the mean PMA film thickness for each dilution and the corresponding replicate ranges, yielding an approximate thickness interval per dilution. PMA A produced the

thickest films, whereas the other four dilutions clustered within a narrower band. In line with Figure 14, where samples A and B exhibited higher charging the practical thickness window is therefore about 0.6–2 µm. Within this window, sample C showed the lowest charging across all accelerating voltages, including the higher settings, suggesting a recommended film thickness of approximately 2.0 µm. The observed minimum in visible charging at an intermediate PMA thickness likely arises because the characteristic electron penetration depth becomes comparable to the film thickness. At an intermediate thickness (~2 µm), the conductive substrate is close enough to influence charge dissipation but not so close that strong field-driven emission effects develop, resulting in a minimum in visible charging. These values are indicative rather than definitive and should be used as guidance when selecting PMA thicknesses that are less prone to charging.

4.2 ToF-SIMS

4.2.1 Evaluation of PMA thickness

All PMA thicknesses were systematically tested and analyzed. For each PMA substrate with excipients, i.e. AP to EP, six locations were measured to ensure representative results. Because the acquisition ran overnight, charging behavior was assessed retrospectively from the acquired images rather than through live observation. Both Figure 15 and Figure 16 shows no indication of charging at either PMA thicknesses.

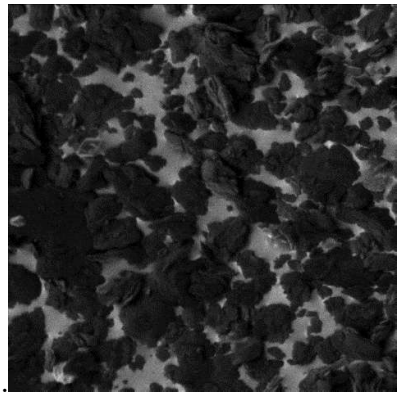

Figure 15: Excipient blend on substrate PMA A (AP).

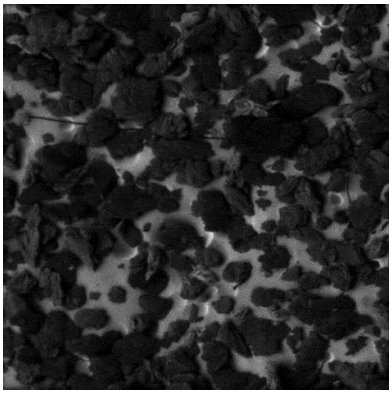

Figure 16: Excipient blend on substrate PMA E (EP).

Analogous to the PMA thickness evaluation in SEM-EDX, an additional sample type was analyzed. Figure 17 presents the spray-dried powder sample with PMA thickness A. The spray-dried powder has not charged in the same way as seen in the SEM-EDX shown in Figure 10.

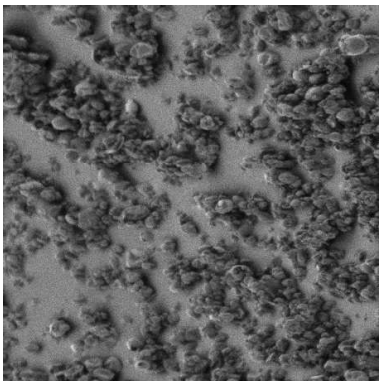

Figure 17: Spray-dried material on PMA A.

For the evaluation of charging effects as a function of PMA thickness, results from the sample with PMA thickness A are compared with those obtained on the thinnest PMA sample (E). Figure 17 shows one of the images acquired on sample with PMA thickness A and Figure 18 shows the sample with PMA thickness E.

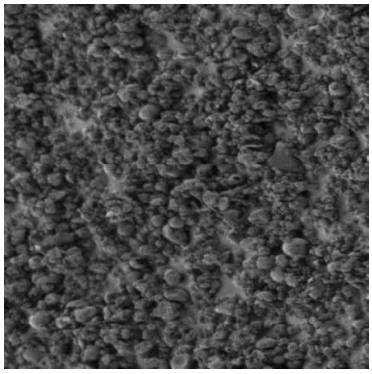

Figure 18: Spray-dried material on PMA E.

As expected, also for the sample with lowest PMA thickness (E) no evidence of sample charging was observed in either Figure 17 nor Figure 18. ToF-SIMS typically shows limited to no visible charging even with thicker PMA layer because most instruments use active charge compensation (low-energy electron flood gun) that continuously neutralizes surface charge during acquisition. Moreover, high particle density can be observed in the analyzed area, suggesting that the PMA thickness E is sufficient to strongly bind enough particles to the substrate even for the thinner PMA thickness.

4.2.2 Peak identification and compositional mapping with IONTOF software

At each image location, a secondary ion mass spectrum (m/z) was acquired. Peak assignment was guided by previously reported characteristic ions for each excipient, which we used as

reference markers. A list of diagnostic mass intervals for these ions was assembled and applied uniformly across the entire spectra obtained for all PMA thicknesses. This approach supported consistent peak identification across replicates and thicknesses. The assigned peaks were then mapped onto the corresponding ToF-SIMS images, enabling color-coded visualization (Table 10) of each excipient's spatial distribution.

Compound	Color
SSG	Red
MCC	Green
MgSt	Dark blue
DCPA	Yellow
PMA	White

Table 10: Color assignment for each component.

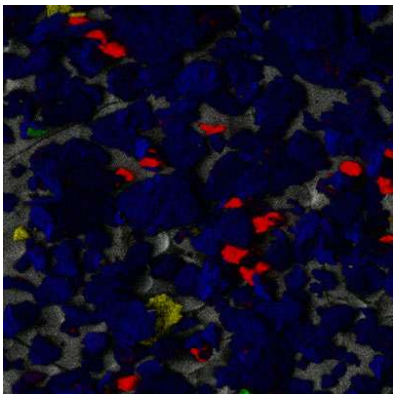

Figure 19: Overlay of excipient distributions on PMA E.

Figure 19 presents the ToF-SIMS overlay, with each component assigned a distinct color to depict its spatial localization within the analyzed spot. The distributions differ markedly among the excipients. This contrast suggests heterogeneity in micro-scale mixing, with certain components forming localized domains and others dispersed more uniformly and possibly smearing on the surface of other particles during blending.

The results presented on the spray-dried powders are limited regarding the exact formulation of the components identified with the ToF-SIMS software on the m/z spectra generated.

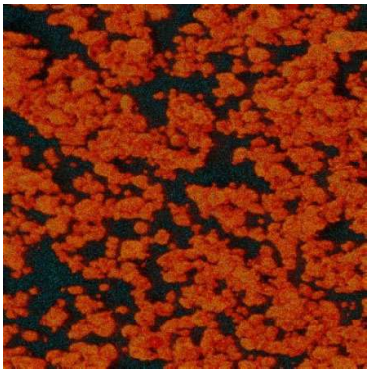

Figure 20: Component-identified overlay of spray-dried powder on PMA A.

Figure 20 shows the overlay of manually selected m/z peaks. The orange color results from the overlay of different m/z peak colors. Due to confidentiality reasons, the exact composition of the spray-dried particles and the putative assignment of the selected m/z peaks cannot be discussed at this stage.

Different samples display their components differently. In the excipient blend, all components were dry mixed and deposited directly onto the substrate. In contrast, for the spray-dried material, the components were mixed prior to spray drying. This processing difference produces the overlay observed in Figure 20 for the spray-dried sample, rather than components appearing in distinct locations such as in Figure 19.

4.2.3 ImagePipeline

Previously mentioned output from ImagePipeline identifies three principal components at a time. Meaning that for the excipient blend the outcome was divided into two different predictions, shown in Figure 21. The results indicate a heterogenicity mixture similarly to the results in Figure 19. Both results from ImagePipeline and the built-in software show similar detection of the elements, validating that the predictions from ImagePipeline corresponds to manual selection.

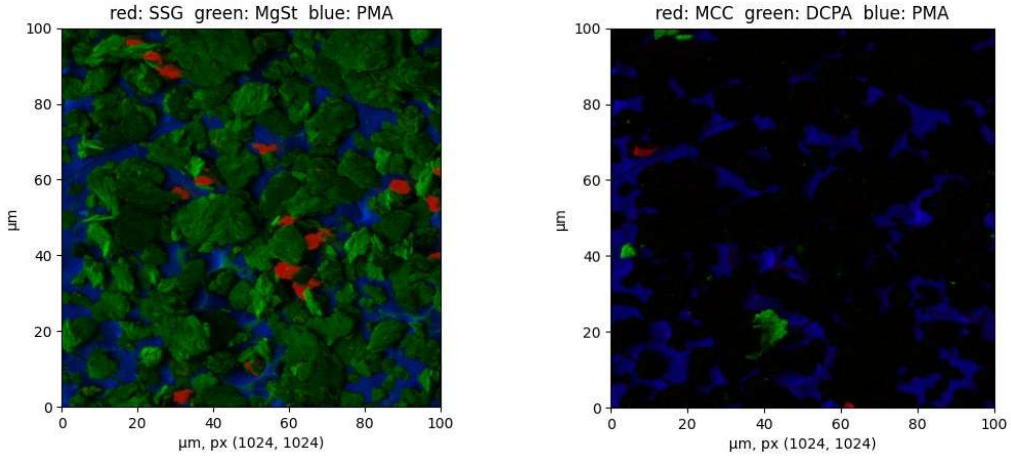

Figure 21: Component prediction overlays (SSG, MgSt, MCC, DCPA, PMA) generated by ImagePipeline.

4.3 Image location

4.3.1 Creating markings for finding the same image location

Figure 22 shows a side-by-side comparison of the fiducial craters in SEM, with the clear visual observation that the thinner PMA substrate (E) shows to have significantly more visible craters than the PMA thickness A.

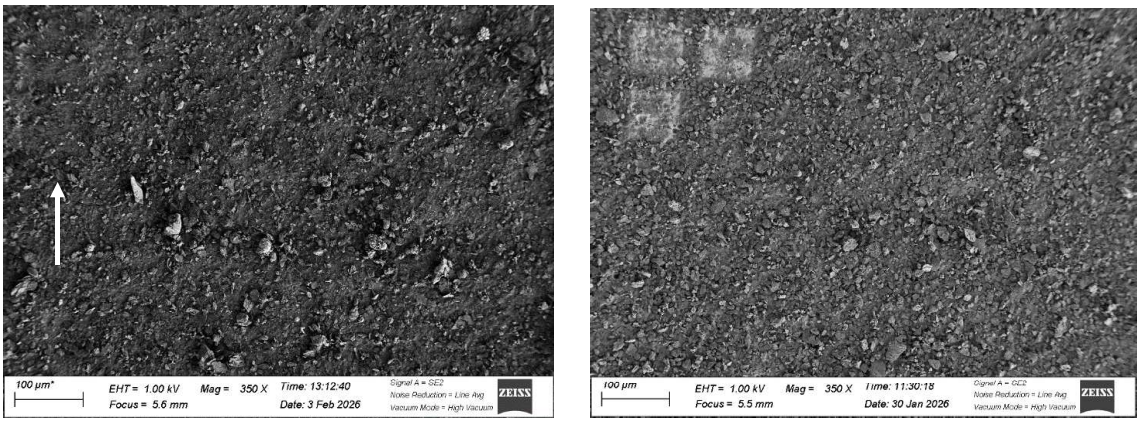

(a) Excipients on PMA A (AP) *(b) Excipients on PMA E (EP)*

Figure 22: Fiducial craters observed in excipient samples at different PMA thicknesses.

The results in Figure 22 show the benefit of using a thinner PMA layer. The improved visual clarity is important for locating the region of interest within SEM and therefore represents an important step in establishing the correlative workflow. The strong signal from the craters comes from the exposed aluminum underneath, which is easy to recognize. This was easier to achieve when the PMA layer was thinner, because less material had to be removed. Thinner layers also led to shallower craters, which were less likely to get refilled by nearby sputtered particles.

From the identification of marked craters each image obtained from ToF-SIMS could be identified and matched to SEM, with the use of a built-in tool that measures the distance within the SEM image. The locations and distribution can be seen in Figure 23 Each white square marks an area for which both ToF-SIMS and SEM analyses were obtained. The larger images are retrieved from SEM, while the smaller, darker images are generated from ToF-SIMS.

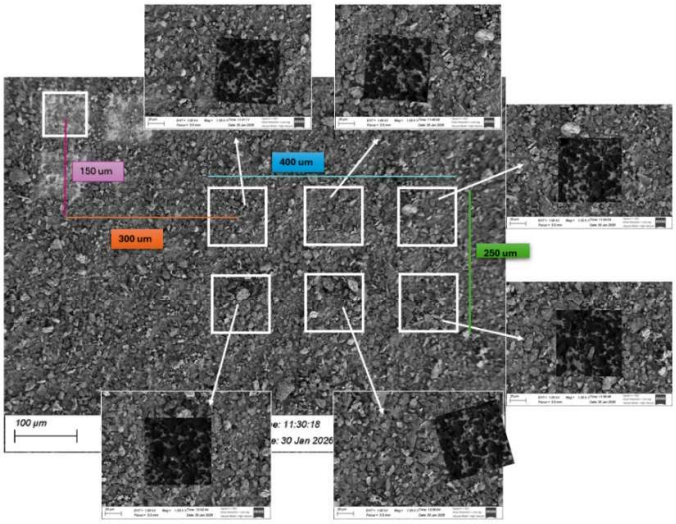

Figure 23: Image locations across SEM and ToF-SIMS datasets.

For each of the six images (marked as squares) a comparison between the two techniques was conducted. With a magnification of 1305x in SEM to cover the entire ToF-SIMS image. A side-by-side comparison between the SEM image and ToF-SIMS image can be seen in Figure 23. However, during the image registration, it was seen that the acquisition angle differs and this needs to be accounted for, especially for the composition analysis and image overlay.

4.3.2 Optimization of acquisition angles within the instruments

After establishing the SEM stage capabilities (including the available tilt range), the standard stage settings were defined as described in Appendix A5. For each image location generated from ToF-SIMS, different acquisition angles were tested and then analyzed as described in Section 3.4.2. Images from the range of angles tested for one of the lactose particles can be seen in Appendix A13. When comparing different angles, keeping the SEM sample flat is not ideal because it produces an image that differs from the ToF-SIMS image.

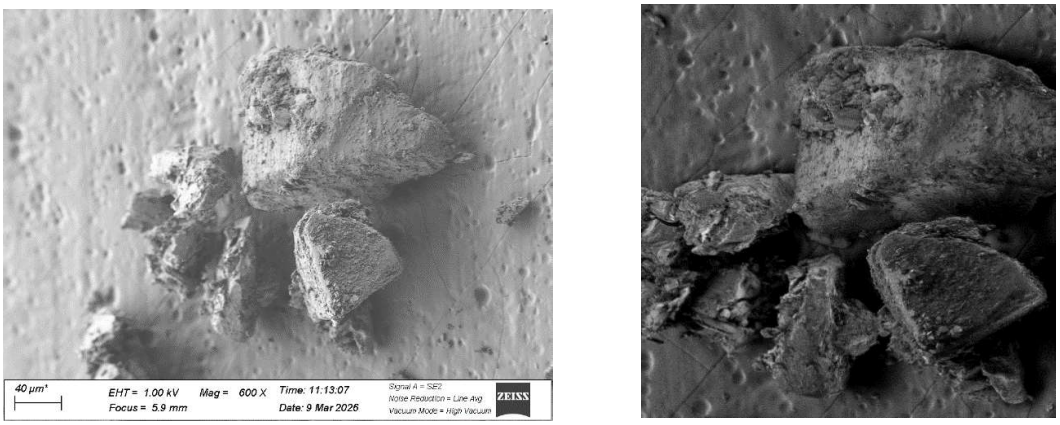

(a) SEM image of area tilted 35 *(b) ToF-SIMS image of area*

Figure 24: Side-by-side comparison of image angles in SEM and ToF-SIMS.

Figure 24 shows the comparison between the tilted sample in SEM with the tilted ion beam in ToF-SIMS. The angle used in Figure 24a is 35°, chosen as the best visual match to the ToF-SIMS image and consistent with the multimodal registration, which identified 35° as the most suitable angle for this sample within the 15–45° range. After testing the 35–45° angle range across different samples, it became clear that the optimal angle may vary depending on the sample type and other factors. Therefore, recommending a single universally optimal angle is not feasible at this stage. Instead, images are acquired across a range of different angles and the best angle is identified by the software (Mireg), and that angle is then used for further evaluation with EDX and for image registration.

4.3.3 Image Registration

Following method optimization and an assessment of how each technique influences data quality, establishing image registration became an important aspect to enable seamless, joint analysis of data from both instruments. This capability summarizes the correlative workflow that is practical, reproducible, and transferable into the work ongoing within AstraZeneca. A first example of the plausible image registration outcome from the developed software (Mireg) can be seen in Figure 25, where one of the large lactose particles was analyzed and used to optimize the model in building the correlative workflow.

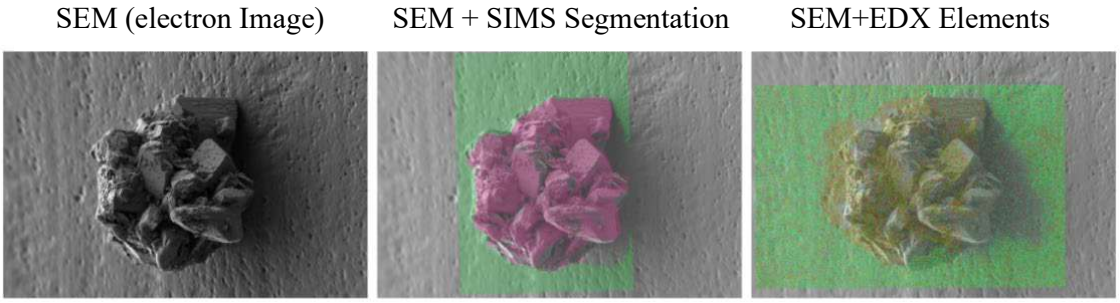

Figure 25: Multimodal image registration and composite overlay.

Figure 25 shows different image registration, in the top middle, the SEM high resolution image is overlayed with the ToF-SIMS output from ImagePipeline where the different principal components are identified.

4.4 Applying the correlative workflow

To assess performance and applicability across pharmaceutical products and use cases, the correlative workflow was applied to multiple sample types following the procedures described in this study. The samples spanned a different sizes, morphologies, and other material characteristics, providing a broad test set to assess whether the workflow is effective across diverse specimens.

4.4.1 Spray dried powder with protein

For a spray-dried powder containing BSA as the model compound, three concentrations were evaluated using the correlative imaging workflow. The workflow enabled reliable image registration and produced an interactive interface that overlays ToF-SIMS molecular components onto high-resolution SEM images, accompanied by density plots showing elemental distributions from EDX analysis for each component. Results are presented for all three concentrations (5%, 10%, 20%).

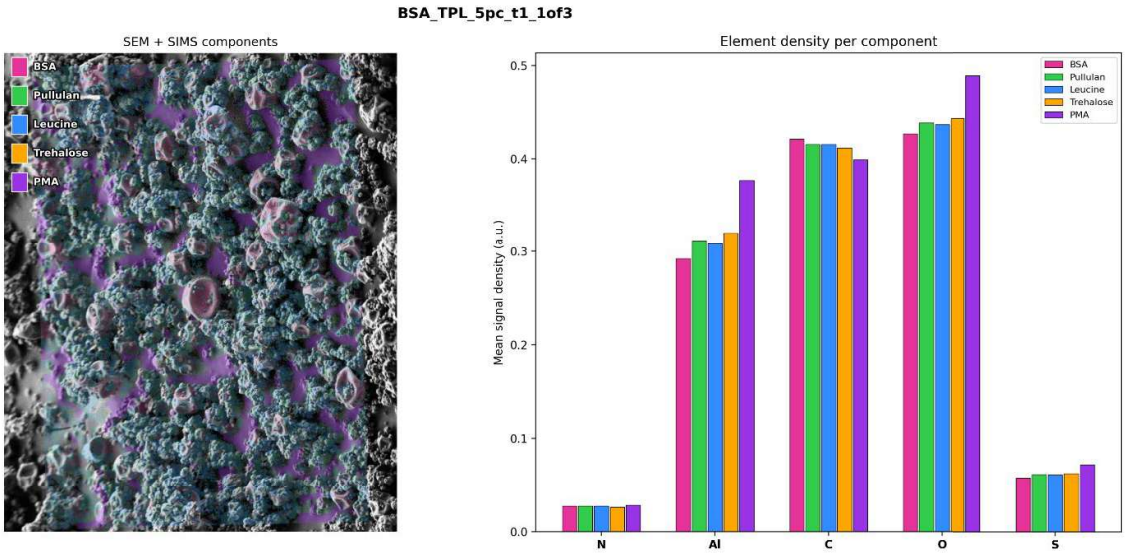

Figure 26: Multimodal registration of the 5% BSA spray-dried powder.

As shown in Figure 26, the high-resolution image on the right indicates that BSA is predominantly localized on larger particles, whereas leucine and pullulan are more associated with smaller particles attached to these larger BSA-rich particles. Trehalose and Pullulan is not detected in the outputs from ImagePipeline. This absence may reflect its confinement within the interior of the larger particles, beyond the ~5 nm analytical depth of ToF-SIMS.

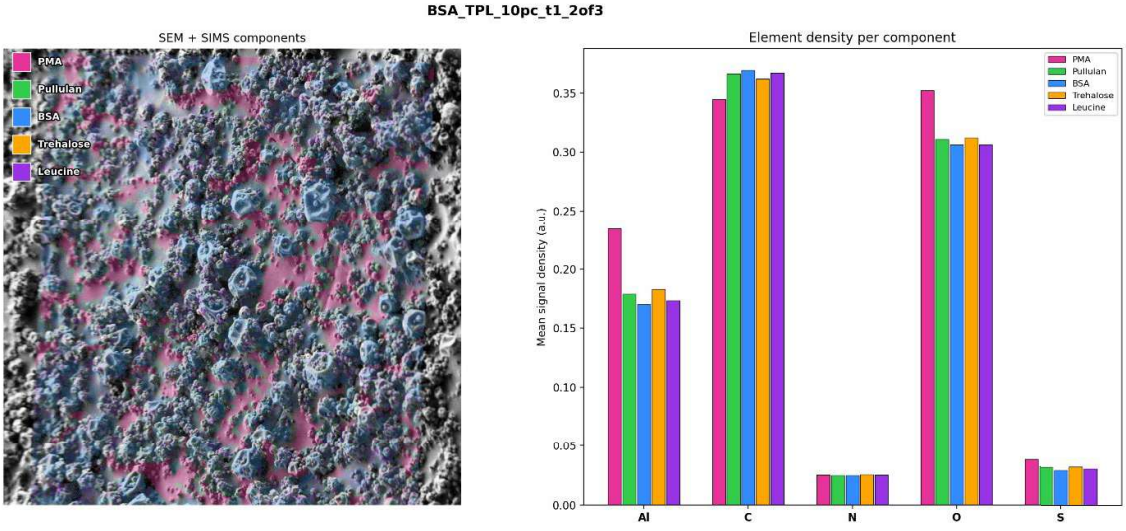

Figure 27: Multimodal registration of the 10% BSA spray-dried powder.

Figure 27 shows a sample with 10% BSA. The overlay indicates higher BSA signal where more particles appear in blue. An even stronger BSA presence is evident in Figure 28 for the 20% sample, consistent with the increased concentration.

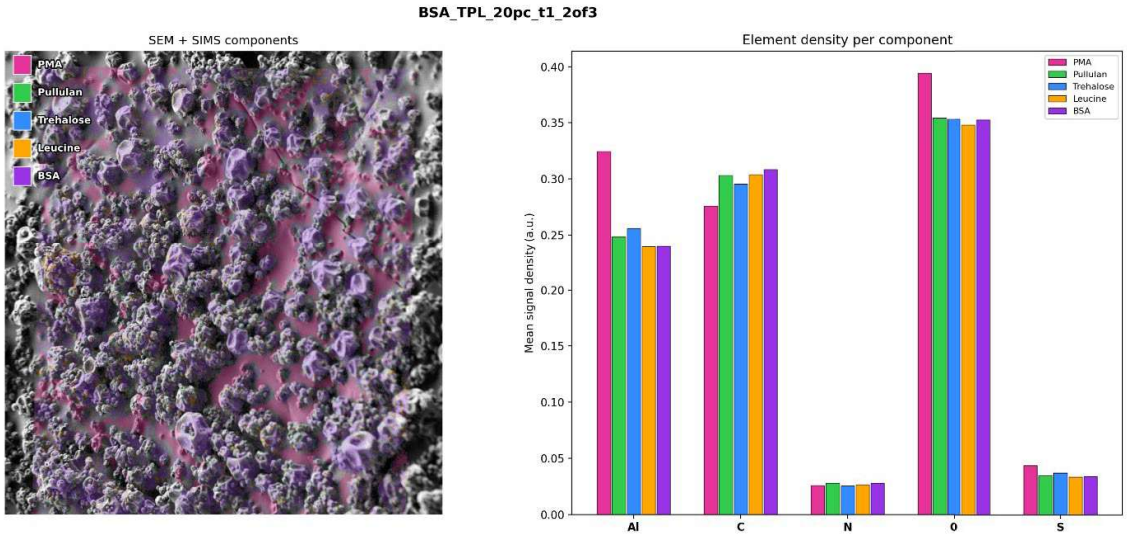

Figure 28: Multimodal registration of the 20% BSA spray-dried powder.

Across all concentrations, the elemental density plots appear similar for all elements within each component. This impression is misleading because the underlying elemental distributions differ. For example, the plots imply equal contributions of nitrogen and sulfur across components, whereas only BSA contains these elements. The discrepancy likely reflects noise and variability in the EDX elemental maps.

It is also important to interpret the density plots correctly: the reported mean density is normalized to the number of pixels assigned to each component. As a result, components can exhibit comparable mean densities even when their areal abundances differ. In the overlays, the BSA signal (purple) occupies a larger area than leucine (yellow), indicating unequal component coverage, while the density plot nonetheless shows similar mean densities due to pixel-based normalization. Since these results can be misinterpreted depending on how the graphs are read, the visualization and analysis approach requires further refinement and development, which was beyond the available time in this study.

4.4.2 Excipient Blend

The Image Registration output presents overlays on the high-resolution SEM image alongside an elemental density chart, seen in Figure 29. The density chart facilitates component-specific interpretation: sodium is most prominent in SSG, magnesium is characteristic of MgSt, and calcium and phosphorus are most associated with DCPA as expected. Aluminum originates from the underlying aluminum substrate beneath the PMA layer. Fluorine (F), nickel (Ni), and sulfur (S) are also present as trace elements in this substrate.

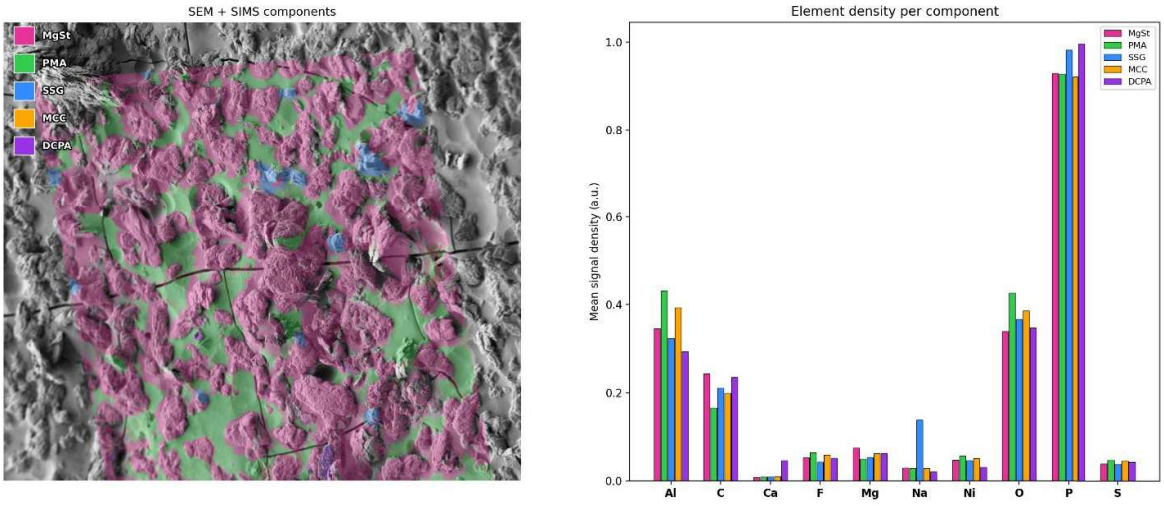

Figure 29: Multimodal image registration of the Excipient blend.

From Figure 29 the left-hand high-resolution image visualizes the spatial distribution of components within the excipient blend. The ImagePipeline output indicates a higher abundance of magnesium stearate (MgSt), with lower-intensity outputs corresponding to the other excipients. There are localized areas attributable to sodium starch glycolate (SSG) and a distinct dicalcium phosphate anhydrous (DCPA) particle. In contrast, microcrystalline cellulose (MCC) is seemingly absent or only at very low levels in this field of view based on the assigned m/z interval list. Magnesium stearate (MgSt) likely delaminates during mixing and coats other particles, this surface coverage explains why, despite a bulk mass fraction of only 1–2%, the majority of particles are classified as MgSt in the ToF-SIMS map.

4.4.3 Ex vivo human skin exposed to $AlCl_3$

Due to the limited number of skin sections analyzed, no reference samples were included. As a result, it was not possible to build an ImagePipeline model, and thus no prediction or separation of background, tissue, ethanol, and $AlCl_3$ components could be performed as originally planned. Consequently, image registration was not carried out. Despite these constraints, analyzing this distinct sample type still yielded useful insights: the workflow appears applicable, and high-resolution SEM images with EDX maps enabled localization of elements. Moreover, the inherent morphological features of the skin facilitated reliable SEM correlation with ToF-SIMS, and the corresponding image locations were readily identified, as shown in Figure 30.

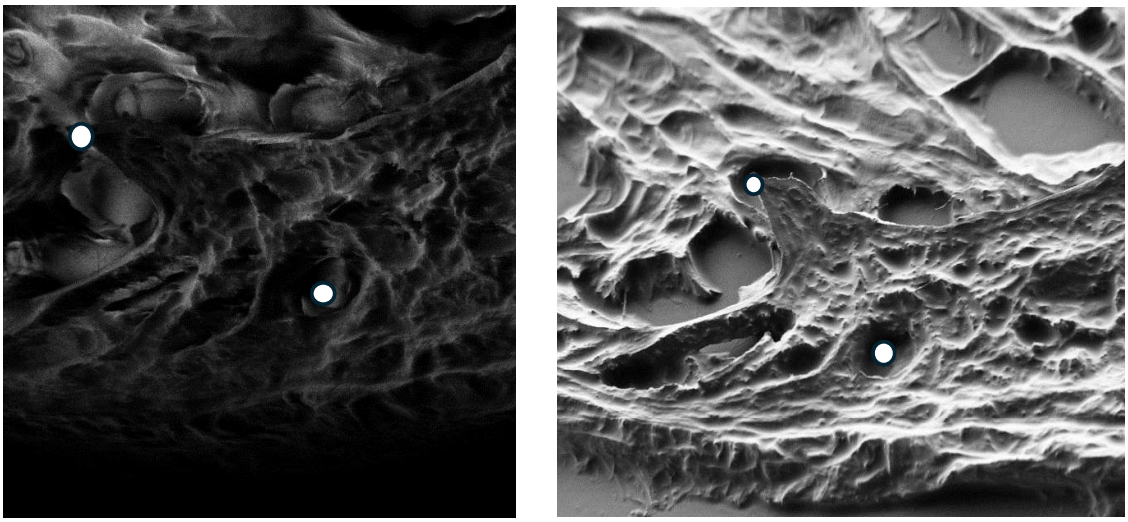

Figure 30: SkinModel images obtain from both ToF-SIMS and SEM.

Another important result is the correspondence of $AlCl_3$ signals in the EDX data. The elemental maps for the image location shown in Figure 31 are provided in Appendix A16. In both sides of the analyzed tissue sections, Al and Cl were detected at similar levels, which is unexpected because only one side of the tissue was exposed to $AlCl_3$. The most plausible interpretation is that $AlCl_3$ permeated the entire sample, penetrating deeply into the tissue. This finding was consistent across two independently analyzed sections. Additionally, EDX indicates a relatively higher abundance of Cl than Al within the sections, as expected based on the fact that $AlCl_3$ contains more Cl than Al. These results can also be visually seen in Figure 31 SEM image, representing the output of the multimodal image registration where the EDX elemental maps are overlayed onto the high-resolution EDX.

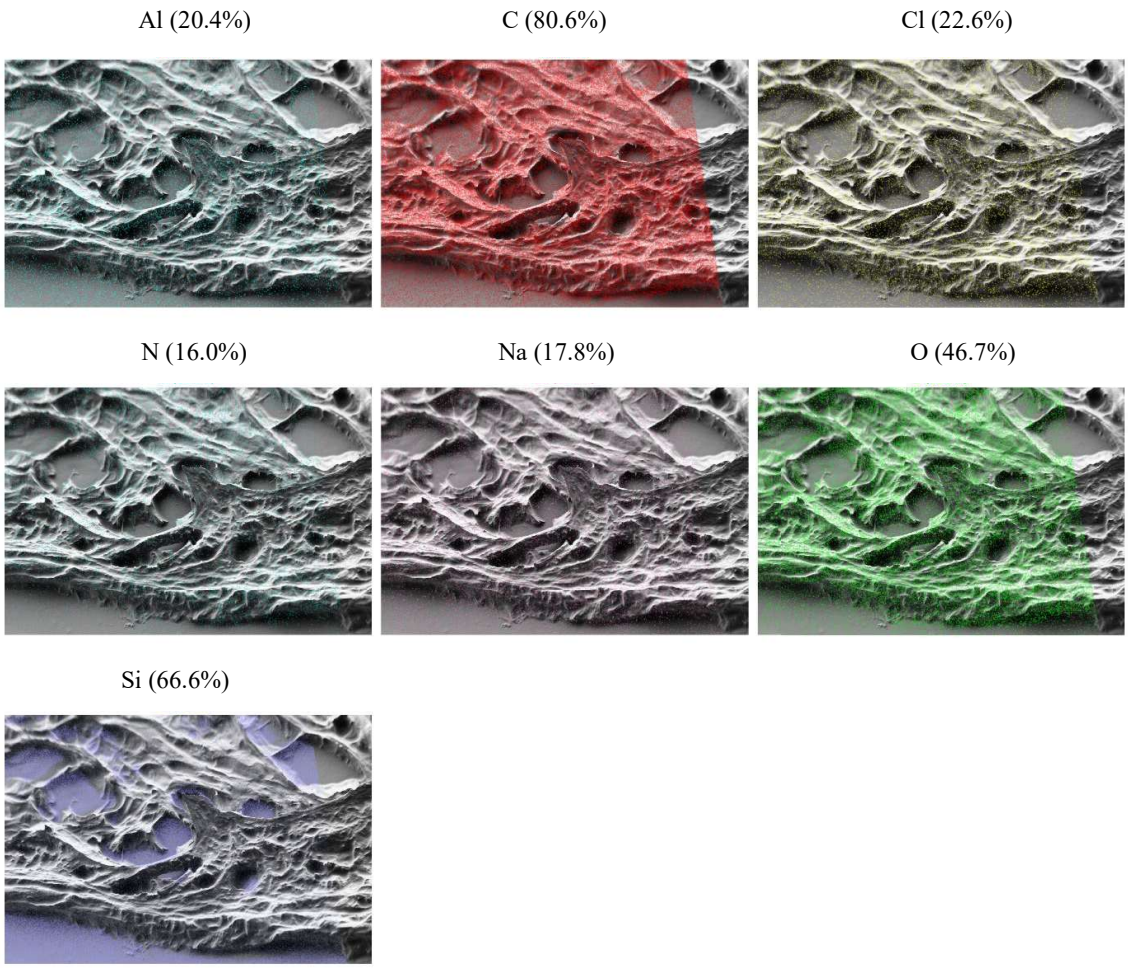

Figure 31: EDX elemental maps registered onto the high-resolution SEM image

The result presented in Figure 31 shows the possibility of using the image registration for a clearer understanding of the locations of certain compounds such as staining, or local accumulation of a compound within the structure of the tissue. However, due to certain time limitations and unavailability of a suitable sample holder, the full image registration was not possible.

5. Discussion

5.1 Method optimization

5.1.1 SEM-EDX

Optimizing instrument parameters is essential to achieve rapid, precise measurements. Establishing settings and understanding sample-specific dependencies helps to provide clear guidance for consistent instrument operation. In scanning electron microscopy (SEM), a critical factor in method optimization is the acceleration voltage of the electron beam, which markedly influences both high-resolution imaging and EDX elemental analysis.

Higher acceleration voltages generally improve the reliability of EDX results, reflected in lower standard deviations and clearer elemental maps. By generating more X-ray photons, the system achieves higher count rates and better statistical precision. However, higher voltages also increase the electron interaction volume and penetration depth, making the underlying substrate more likely to contribute to the detected signal. This contribution can bias the reported elemental weight percentages and must be accounted for in image registration, data interpretation, and final conclusions. Acceleration voltage also affects high-resolution SEM imaging. Elevated voltages can amplify surface charging, which may appear as bright spots and obscure true surface morphology and can increase beam-induced damage in sensitive materials. Beam-induced damage can appear as loss of fine detail and other irreversible changes of surface microstructure. In sensitive materials such as skin tissue or cells, the electron beam may trigger chemical rearrangements, bond breakage, and mass loss. Because these materials have distinct microstructural features, it is critical to preserve them by minimizing charge-related artefacts and avoiding exposure conditions that risk feature removal. Balancing these tradeoffs (EDX sensitivity and precision versus spatial resolution, charging artifacts and beam damage), is central to selecting appropriate operating conditions for each sample.

Switching from high vacuum to variable pressure (VP) mode is sometimes necessary to achieve the acceleration voltages required for certain elements in the EDX analysis. However, this change introduces a trade-off: VP conditions can slightly alter image characteristics relative to high-resolution SEM, reducing the precision of image correlation and overlay. Where feasible, achieving higher voltages by applying a conductive coating can reduce reliance on VP mode. This approach can streamline workflow and improve data quality by lowering charging, increasing count rates, and enhancing statistical precision, yielding more reliable SEM and EDX measurements and by supporting better spatial resolution, particularly in EDX mapping.

5.1.2 ToF-SIMS

Time-of-flight secondary ion mass spectrometry (ToF-SIMS) operates within an established workflow, though certain parameters such as surface potential can vary across samples. Polymethacrylate (PMA) has already been integrated successfully in ToF-SIMS workflows,

so its basic suitability is known. However, it was still an important aspect in method optimization to evaluate multiple PMA thicknesses. In the results presented, PMA thickness showed no discernible impact on image resolution, mass-interval spectra, or sample charging in ToF-SIMS.

The accurate molecular identification from the ToF-SIMS outputs relies on careful calibration and processing of the m/z spectra. It is essential to apply the same processing to both the sample and its reference components. This enables reliable identification within ImagePipeline: the model is trained on references to distinguish background from reference signals based on their m/z spectral patterns. This makes it possible for the model to predict and distinguish each component in the overall sample.

5.2 Correlative workflow

5.2.1 Build of the correlative workflow

The optimization outcomes for both modalities demonstrate strong feasibility for a correlative analytical workflow. Scanning electron microscopy coupled with energy-dispersive X-ray spectroscopy (SEM-EDX) offers complementary strengths: high spatial resolution, site specificity, and rapid acquisition of elemental distributions. In parallel, time-of-flight secondary ion mass spectrometry (ToF-SIMS) delivers molecular-level information with exceptional surface sensitivity (approximately 5 nm analytical depth), enabling detection and tentative identification of complex species. Together, these capabilities create a robust basis for co-registered elemental and molecular analysis.

A critical prerequisite for correlative analysis is sample preparation that is compatible with both instruments. This work prioritized establishing a polymethacrylate (PMA) adhesive layer on an aluminium substrate that minimizes artefacts while maintaining particle adherence. The results indicate that thinner PMA layers reduced charging in SEM, improving high-resolution imaging, while still providing sufficient adhesion. This balance was essential to enable sequential measurements on the same physical specimen without compromising data quality in either modality.

Once cross-instrument compatibility was achieved, the next requirement was reliable site localization across SEM-EDX and ToF-SIMS. Introducing fiducial craters proved effective for spatial registration. In ToF-SIMS, the precise distances from each crater to the image fields and between fields was recorded, then used those measurements to relocate the same regions in SEM-EDX. For consistent crater formation, extended sputtering at maximum long-pulse intensity in ToF-SIMS was required. To minimize the risk of redeposition onto regions of interest (which could confound subsequent SEM analysis), craters should be created either before imaging the target areas or placed at a sufficient offset from those areas.

Mechanical constraints also influence reproducibility. The SEM stage supports tilt only within specific orientations, so the sample must be mounted on the SEM holder exactly as

specified (see Appendix) to ensure that the instrument can reach the required tilt and working-distance geometry for both imaging and EDX acquisition. With these practices in place, cross-modal relocation and comparison of morphological and compositional features were straightforward in high vacuum (HV) SEM.

Variable pressure (VP) SEM introduces an additional consideration. Under VP conditions, fiducial craters and subtle surface features are less distinct, making registration more difficult. An efficient procedure is to perform localization and reference imaging in HV SEM, capture a high-resolution image at the correct site, then switch to VP without moving the stage to conduct EDX, before advancing to the next site. This approach maintains positional fidelity while leveraging VP to mitigate charging when necessary.

Finally, projection differences must be addressed to achieve high-quality image overlays. During evaluation of acquisition angles in SEM, the recommended alignment angle can vary not only between samples but also across locations on the same sample, likely due to local topography and mounting tolerances. Consequently, angle optimization should be treated as an iterative step in the workflow: test a small set of candidate tilt settings per region, select the configuration that maximizes feature correspondence. Incorporating this step improves overlay accuracy and strengthens the interpretability of correlative datasets.

5.2.2 Applying the correlative workflow

To establish a correlative workflow that is both practical and efficient, the built workflow was systematically evaluated and its performance across diverse sample types demonstrate scope and generalizability. The test set comprised three distinct matrices: spray-dried powder containing biologics, an excipient blend, and a skin model. These samples were chosen to span markedly different morphologies, conductivities, and surface chemistry. Given these contrasts, divergent outcomes were anticipated and, in several cases, observed.

A key finding concerns the relationship between particle size and the suitable imaging/overlay angle. Empirically, smaller particles required less tilt to achieve satisfactory correspondence between SEM-EDX and ToF-SIMS images; thus, screening a lower-angle range can be sufficient for fine particulates. In contrast, larger particles (e.g. lactose granules) often benefited from higher tilt angles, with values approaching ~45° yielding improved alignment and feature visibility. This size-dependent guidance can streamline angle selection and reduce iterative repositioning.

Cross-sample application also highlighted instrument-setting constraints, particularly those imposed by charging in SEM. For example, spray-dried biologic powders exhibited a lower tolerance for high acceleration voltages than the excipient blend, necessitating adjustments such as reduced kV or a greater reliance on variable pressure and increasing the pressure in VP mode. These adaptations were essential to maintain image quality, EDX fidelity, and spatial registration without introducing artefacts.

The use of fiducial markers is valuable and has been an effective way to relocate the same imaging area across instruments. However, for samples such as tissue (and likely cells), fiducials can risk damaging the matrix and, in these cases, it is preferable to rely on the sample's own characteristic features for correlative alignment. Biological tissues also behave differently in SEM–EDX, making high-resolution imaging challenging; the achieved resolution was not optimized. This should be considered when interpreting results, as tissues lack the sharp edges and discrete boundaries typical of particulate samples, which complicates focusing, charge management, and feature recognition.

5.2.3 Challenges

Establishing the correlative workflow revealed several practical challenges that influenced both data quality and operational efficiency. Selecting a suitable substrate was a prominent early hurdle during method development. Although this did not ultimately impede application of the workflow to real samples, it underscored the sensitivity of correlative imaging to surface chemistry and topography, particularly when balancing signal quality across modalities.

A more consequential limitation was the mismatch in acquisition angles between the instruments. Stage tilting in the SEM partially mitigated this discrepancy, improving spatial correspondence, but it did not deliver a fully ideal match. In practice, multiple tilt angles may need to be evaluated empirically for each sample type to achieve satisfactory alignment. As discussed in Section 5.1.1 the perceived angle offset appears to diminish with decreasing sample size, though this observation may reflect the specific specimens tested and needs to be further evaluated. Until a generalized solution is established, angle optimization remains a source of residual registration error and adds iteration time to the workflow.

The requirement to operate EDX in variable-pressure (VP) mode posed an additional challenge. Switching to VP necessitates adjustments within the vacuum chamber and has been observed to introduce small positional shifts. These shifts complicate guarantees that the EDX map and the preceding high-resolution SEM image originate from precisely the same field of view. While landmark-based overlays reduce the impact of minor misalignments and preserve the interpretability of the correlative results, the mode change adds complexity and time. A potential mitigation is the use of conductive coatings to stabilize charging and enable acquisition of EDX and high-resolution SEM under identical conditions, thereby eliminating the VP switch. This approach, however, must be balanced against the risk that coatings alter surface chemistry or obscure signals from light elements.

Taken together, these considerations highlight that correlative performance depends not only on algorithmic registration but also on physical parameters, substrate choice, geometric alignment, and chamber operating mode, that can introduce subtle but meaningful variability. Iterative calibration of tilt and a deliberate strategy for charge management (VP versus coating) are likely to yield the most consistent outcomes. One practical implication is the value of designing experiments with internal landmarks and redundancy in image fields to

buffer against small shifts, while planning sufficient instrument time for angle scouting when sample geometry is unfamiliar.

Another potential challenge is the requirement for reference materials corresponding to all components in the sample. This reliance becomes especially important when using tools that automatically sort images, follow specialized image routines, or separate mixed signals across different types of data. In the analysis of the ex vivo skin model, the absence of validated references for tissue constituents, ethanol, and $AlCl_3$-related species limited the ability to train or validate the ImagePipeline model and to separate background from analyte signals with confidence. As a result, interpretation relied more heavily on assignments and qualitative assessment, increasing uncertainty and reducing generalizability.

5.2.4 Benefits

When integrated, the correlative workflow enables co-registration of high-resolution morphological information from SEM, elemental distributions from EDX with molecular and fragment ion contrasts from ToF-SIMS, which enhances the interpretability of microstructural features, interfaces, and compositional gradients. In practice, EDX provides rapid, spatially localized maps of elements that anchor the morphology and identify different phases, while ToF-SIMS contributes high chemical specificity, surface sensitivity and selective information on organic molecules, lipids, polymers, and trace additives. Beyond acquisition, ToF-SIMS benefits from established processing and classification workflows such as ImagePipeline, supporting spectrum calibration, peak picking, feature selection, and supervised model training for robust component assignment (for example, distinguishing background, excipients, active ingredients, and contaminants against a set of references). Combining both techniques makes it easier to tell which materials are present and to understand what happens at their boundaries, because elemental maps (from SEM–EDX) and molecular maps (from ToF-SIMS) either confirm each other or highlight differences that need attention. This integration strengthens conclusions compared with analysing modalities in isolation, because hypotheses can be tested against orthogonal evidence and ambiguous signals can be resolved through agreement (or tension) between elemental and molecular readouts.

Applied to pharmaceuticals, the workflow generalizes well across powders and blends used in drug development, enabling assessment of dispersion, component co-localization, morphology, surface enrichment, and process heterogeneities that may affect flow, compaction, and dissolution Extending the same framework to biological tissues demonstrates broader utility. High-resolution SEM provides detailed morphology, enabling clearer visualization of the biological structures. Elemental maps from EDX can localize stains or salts and, where compounds contain distinctive heteroatoms, can support drug tracking, while recognizing that EDX's lower spatial resolution may limit sensitivity and specificity compared with ToF-SIMS. Conversely, ToF-SIMS maps can track drugs, metabolites, or lipids with superior surface sensitivity and higher lateral resolution and can also detect stains or salts; however, peak assignment may be complicated by isobaric

fragments, where complementary EDX information can help resolve ambiguity. In settings where both instruments are routinely used, integrating them through a shared coordinate system and common analysis framework consolidates effort, improves efficiency, and yields richer, cross-validated insights from the same sample areas.

5.3 Further evaluation and prospects

Looking ahead, several refinements would strengthen the correlative workflow and support broader application beyond pharmaceuticals. First, routine practice for geometric alignment should be standardized by defining a clear procedure for SEM stage tilting, including angle scouting, verification, and acceptance criteria. A repeatable tilt protocol will shorten setup time and improve cross-modality registration across diverse sample types. Second, charge management merits systematic evaluation. Applying an ultrathin conductive coating by sputter coating could enable higher acceleration voltages in high vacuum mode, eliminating reliance on variable-pressure mode for highly charging samples, thereby reducing mode switches and the positional shifts they can introduce. Any coating strategy should be validated to confirm that it does not obscure low elemental signals. Third, the computational pipeline should be advanced to increase registration precision and robustness. Improving the interface between ImagePipeline outputs and SEM fields of view, through fiducial-free feature matching, distortion correction, and quantitative overlap metrics, would minimize residual misalignment. Even small registration errors can be consequential near interfaces or when features approach the resolution limit.

After completion of the workflow through multimodal image registration, a post-assessment was conducted to understand how acquisition parameters might influence image registration quality and downstream readouts. This analysis informs future optimization rather than the primary results. In particular, the effects of EDX acquisition time and spatial resolution on elemental composition maps were examined using three acquisition durations and resolutions (approximately 3 minutes, 15 minutes, and 1 hour). Comparison of the multimodal registration outputs in Figure 32 it indicated that acquisition time (and the associated count resolution) can materially affect the final outputs, highlighting a trade-off between precision and throughput that should be considered in future studies.

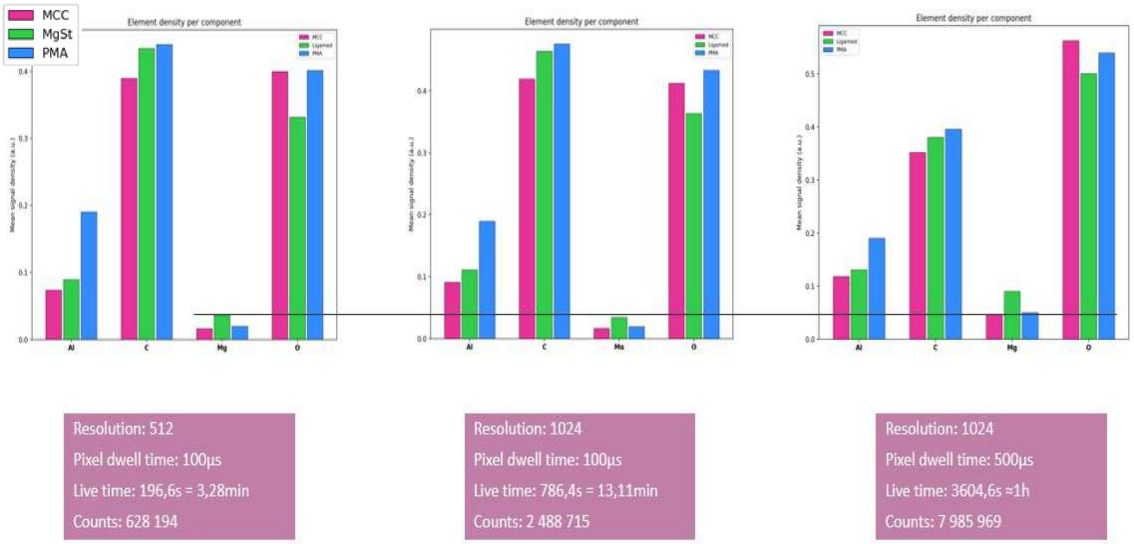

Figure 32: Elemental density per component for different acquisition times.

Comparing the graphs indicates that longer EDX acquisition times yield clearer trends, most notably a stronger association of Mg with MgSt in the domain identified by ToF-SIMS and ImagePipeline. An additional difference emerges for oxygen: at 15 minutes, PMA appears to carry the highest O signal, whereas at 1 hour the highest O signal is attributed to MCC. This brief assessment underscores the need for a more systematic evaluation of acquisition time and related settings, as these parameters influence both the quantitative outputs and the inferred trends, and therefore are critical for improving reliability. In EDX/SEM mapping, binning combines pixels to improve signal-to-noise, at the cost of spatial resolution. However, applying binning to the EDX maps did not affect the image-registration outcome within the tested range. Another plausible future direction is to apply noise-reduction filters to the EDX data, improving signal-to-noise and enabling clearer element detection for each component. Where a quick trial run of using gaussian filtration on the Mg elemental map obtained from EDX showed the possibility of having less noise and more accurate output, shown in Figure 33.

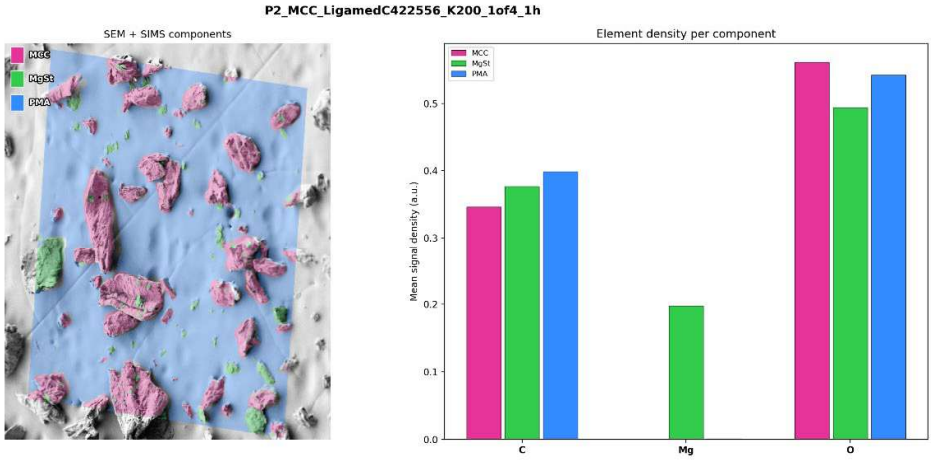

Figure 33: Mireg output with filtered Mg elemental map

Expanding the reference library is also a priority for reliable supervised classification and spectral interpretation, particularly for complex matrices such as tissue. A minimal set that includes tissue-only, solvent-only, analyte-only, and spiked controls would enable basic model training, calibration, and validation. With these foundations, the workflow can be generalized to additional contexts, ranging from biological tissues and cell preparations to polymer composites, by maintaining consistent alignment, charge control, and reference standards. Finally, extending the correlative framework to integrate other spatial modalities (for example, Raman or IR micro spectroscopy, AFM, or X-ray microanalysis) within a shared coordinate system could yield richer, orthogonal evidence. Together, these future developments aim to streamline routine operation, enhance reproducibility, and increase the interpretability of co-registered elemental and molecular maps across a wider spectrum of applications.

6. Conclusion

This thesis developed and demonstrated a correlative workflow that integrates SEM–EDX elemental mapping with ToF-SIMS molecular imaging to analyze microstructure and composition within the same sample areas. The workflow was evaluated on pharmaceutical powders (including spray-dried powder containing proteins and an excipient blend) and extended to an ex vivo skin model, showing that coordinated acquisition and harmonized processing can deliver complementary insights that neither modality provides alone. Key challenges were identified, geometric alignment across instruments, charge management, limited reference materials for complex matrices, and operational mode switching, and practical mitigations were outlined. Despite these constraints, the results confirm that correlative SEM–EDX/ToF-SIMS is a feasible, informative approach for mapping interfaces, distributions, and component identities across diverse sample types. The methods, observations, and recommendations presented here provide a foundation for routine application and future expansion of the workflow to broader materials and biological contexts.

Bibliography

1. *Pharmaceutical Particle Engineering via Spray Drying.* Vehring, R. 2008, Pharmaceutical Research, Vol. 25, pp. 999-1022.
2. *Imaging of Crystalline and Amorphous regions using Time-of-Flight: Secondary mass spectrometry (ToF-SIMS): Application to Pharmaceutical Materials.* Luras, A. et al. s.l. : American Chemical Society, 2016. https://doi.org/10.1021/acs.analchem.5b02621.
3. *High spatial resolution ToF-SIMS imaging and image analysis strategies to monitor and quantify early phase separation in amorphous solid dispersions.* Paladino, E. et al. 2022, International Journal of Pharmaceutics, Vol. 628.
4. *Sample Preparation of Biological Tissues and Cells for the Time-of-Flight Secondary Ion Mass Spectrometry.* Gulin, A. et al. 2020, Journal of Analytical Chemistry, Vol. 75.
5. *Advancement in ToF-SIMS imaging for life science.* Jia, F. et al. 2023, Frontier in Chemistry. PMC10483116.
6. *Quantification of percolating Ni in fuel electrodes of solid oxide fuel cells using EDX and low voltage SEM.* Labbe, M. et al. 2025.
7. Sputter coating for SEM: how this sample preparation technique assists your imaging. [Online] ThermoFisher SCIENTIFIC. https://www.thermofisher.com/se/en/home/global/forms/industrial/sputter-coating-sem.html.
8. *Assessing the potential of ToF-SIMS as a complementary approach to investigate cement-based materials — Applications related to alkali–silica reaction.* Bernard, L. and Leemann, A. 2015, Cement and Concrete Research, Vol. 68.
9. *SEM-EDX analysis and TOF-SIMS 3D imaging of a textile/rubber interface undergoing fatigue loading.* Valantin, C. et al. 2016, Vol. 360.
10. *Development of correlated FIB-ToF-SIMS and SEM-AM methods for the search for, and characterisation of, enriched uranium particles.* Rickard, W. et al. s.l. : EPJ Web Conf, 2026, Vol. 349.
11. *ToF-SIMS 3D imaging unveils important insights on the cellular microenvironment during biomineralization of gold nanostructures.* Singh, A.V. et al. 261, s.l. : Sci Rep, 2020, Vol. 10.
12. *A correlative method to quantitatively image trace.* Yedra, L. et al. 2021.
13. *ToF-SIMS and SEM-EDS analysis of the surface of chosen bioindicators.* Szynkowska, M.I. et al. 2008, Applied surface science, Vol. 255.
14. *Image fusion combining SEM and ToF-SIMS images.* Milillo, T. et al. 2014.
15. *First use of data fusion and multivariate analysis of ToF-SIMS and SEM image data for studying deuterium-assisted degradation processes in duplex steels.* Sobol, O. et al. 2016.
16. *Drug discovery and development in Phamraceutical industry.* Dayley, J.W. s.l. : Britannica, 2025.
17. *Pharmaceutical therapeutic substances.* s.l. : Britannica, 2025.
18. Drug substance. *National cancer institute.* [Online] https://www.cancer.gov/publications/dictionaries/cancer-terms/def/drug-substance.
19. Drug substance vs drug product. *EMMA international.* [Online] 2024. https://emmainternational.com/drug-substance-vs-drug-product/.

20. *Rapid determination of the active pharmaceutical Ingredient (API) content of suspension formulations using Broadband acoustic resonance dissolution spectroscopy (BARDS).* O'Mahoney, N. et al. 2025, International Journal of Pharmaceutics, Vol. 674.
21. *Excipients in drug delivery systems: A comprehensive review of approved inactive ingredients for human ophthalmic formulations.* Arribada, R.G. et al. 2025, European ournal of Pharmaceutics and Biopharmaceutics, Vol. 208.
22. *Chapter 2 - Current Developments in Excipient Science: Implication of Quantitative Selection of Each Excipient in Product Development.* Kar, M. et al. 2019, Basic Fundamentals of drug delivery.
23. Magnesium Stearate. *Sigma Merck.* [Online] https://www.sigmaaldrich.com/GB/en/product/aldrich/415057?utm_source=bing&utm_medium=cpc&utm_campaign=780+material+science_dsa_WW_%28bing+ebizpfs%29&utm_id=627278667&utm_content=1164384675095193&msclkid=d5e881e03e6c19216b4be8be97152a5e&utm_term=sigmaaldri.
24. *Biopharmaceutical aspects and implications of excipient variability in drug product performance.* Zarmpi, P. et al. 2017, European Journal of Pharmaceutics and Biopharmaceutics, Vol. 111.
25. Microcrystalline Cellulose Powder: Properties, Uses, and Benefits in Pharmaceutical Applications. *Amster.* [Online] 2023. https://amstermicrocell.in/microcrystalline-cellulose/.
26. *Monetite, an important calcium phosphate compound–Its synthesis, properties and applications in orthopedics.* Zhou, H. et al. 2021, Acta Biomaterialia, Vol. 127.
27. Zahid, A. *Calcium Phosphates in Biological and Industrial Systems.* 1998.
28. *A comprehensive understanding of disintegrants and disintegration quantification techniques: From the perspective of tablet microstructure.* Liu, Z. et al. 202388, Journal Drug Delivery Science and Technology, Vol. 88.
29. *Monitoring blending of pharmaceutical powders with multipoint NIR spectroscopy.* Scheibelhofer, O. et al. 2012, AAPS J.
30. *An investigation into the effects of excipient particle size, blending techniques and processing parameters on the homogeneity and content uniformity of a blend containing low-dose model drug.* Alyami, H. et al. 2017.
31. *Spray drying of pharmaceuticals and biopharmaceuticals: Critical parameters and experimental process optimization approaches.* Ziaee, A. et al. 2019, Vol. 127.
32. *Innovative Drying Technologies for Biopharmaceuticals.* Sharma, A. et al. 2021, International Journal of Pharmaceutics, Vol. 609.
33. *Recent progress in drying technologies for improving the stability and delivery efficiency of biopharmaceuticals.* Emami, F. et al. 2022.
34. *Evaluation of nano spray drying as a method for drying and formulation of therapeutic peptides and proteins.* Haggag, Y.A. and Faheem, A.M. 2015, Frontiers in Pharmacology.
35. TenSkin (tm). *Xtenbio.* [Online] https://ten-bio.com/.
36. *A human ex vivo skin model breaking boundaries.* Wurbs, A. et al. 2024.
37. Genoskin & Argenx showcase, human-based nam platform. *Genoskin.* [Online] Genoskin. https://genoskin.com/.

38. Stokes, D.J. *Principles and Practice of Variable Pressure/Environmental Scanning Electron Microscopy (VP-ESEM).* s.l. : Wiley, 2008.
39. Luyk, E. Backscattered Electrons in SEM Imaging. *ThermoFisher Scientific.* [Online] 2019. https://www.thermofisher.com/blog/materials/backscattered-electrons-in-sem-imaging/.
40. *Chapter 19 - Reverse osmosis membrane fouling and its physical, chemical, and biological characterization.* Ashfaq, Y.M. and .Al-Ghouti, M.A. 2022, 60 Years of the Loeb-Sourirajan Membrane.
41. Secondary Electrons in SEM: Unlocking Surface Insights at the Nanoscale. *NanoScience Instruments.* [Online] https://www.nanoscience.com/blogs/secondary-electrons-in-sem-unlocking-surface-insights-at-the-nanoscale/.
42. *AZtec User Manual.* s.l. : Oxford Instruments, 2013.
43. SEM Accelerating Voltage: Impact on Resolution. [Online] 2024. https://elementpi.com/sem-voltage-res/#:~:text=Accelerating%20voltage%20refers%20to%20the%20energy%20imparted%20to,beam%20and%20the%20resolution%20of%20the%20resulting%20images..
44. Why Use Low Accelerating Voltage for SEM Imaging? *NanoScience Instruments.* [Online] https://www.nanoscience.com/blogs/why-use-low-accelerating-voltage-for-sem-imaging/.
45. *Optimization of measurement conditions in SEM microscopy – a case study.* Bielicka, M. et al. Measurement, Vol. 253.
46. *Microscopy Methods for Biofilm Imaging: Focus on SEM and VP-SEM Pros and Cons.* Relucenti, M. et al. 2021.
47. Gaskin, J. Variable Pressure - Scanning Electron Microscopy (VP-SEM). *NASA.* [Online] 2022. https://ntrs.nasa.gov/citations/20220018942.
48. Fundamentals of Scanning Electron Microscopy in Life Science Research. *Zeiss.* [Online] https://url.de.m.mimecastprotect.com/s/bRDMCx6pByCOxJBD2H8fAHyJFm9?domain=zeiss.com.
49. Scimeca, M. et al. *Energy Dispersive X-ray (EDX) microanalysis: A powerful tool in biomedical research and diagnosis.*
50. X-ray Interactions with Matter. *Radiologica.* [Online] 2021. https://radiologica.org/knowledge-base/interactions-with-matter/#:~:text=The%20Compton%20effect%20refers%20to%20interactions%20between%20an,scatters%20in%20a%20different%20direction%20with%20less%20energy..
51. Electron Beam Energy. *ThermoFisher Scientific.* [Online] https://www.thermofisher.com/se/en/home/materials-science/learning-center/applications/sem-technology-electron-beam-voltage.html.
52. From Surface to Depth: How Accelerating Voltage Affects SEM Imaging. *NanoScience Instruments.* [Online] https://www.nanoscience.com/blogs/from-surface-to-depth-how-accelerating-voltage-affects-sem-imaging/.
53. Energy Dispersive Spectroscopy. *Myscope.* [Online] https://myscope.training/EDS_Intensity_basics.
54. Goldstein, J.I. et al. *Scanning Electron Microscopy and X-ray Microanalysis.* s.l. : Kluwer Academic / Plenum Publishers, 2003.

55. *Chapter 10 - Physicochemical characterization of nanomaterials: size, morphology, optical, magnetic, and electrical properties.* Barhoum, A. and Garcia-Betancourt, M.L. 2018, Emerging Applications of Nanoparticles and Architecture Nanostructures.
56. Gold vs Platinum: Choosing the Right Coating for SEM Imaging. *NanoScience.* [Online] https://www.nanoscience.com/blogs/gold-vs-platinum-choosing-the-right-coating-for-sem-imaging/.
57. How to Combat Electric Charge Buildup in Scanning Electron Microscopy. *nanoScience Instruments.* [Online] https://www.nanoscience.com/blogs/how-to-combat-electric-charge-buildup-in-scanning-electron-microscopy/.
58. Sputter Coater Principles. *Electron Microscopy Sciences.* [Online] https://www.emsdiasum.com/docs/technical/datasheet/sputter_coating.
59. How thick is sputter coating? Achieve Precision Thin Films from Nanometers to Microns. *Kintek Solution.* [Online] https://kindle-tech.com/faqs/how-thick-is-sputter-coating#:~:text=In%20short%2C%20sputter%20coating%20is%20a%20thin-film%20deposition,not%20for%20creating%20thick%2C%20bulk%20layers%20of%20material..
60. Introduction to metal coating technology for electron microscopy. *NanoScience.* [Online] NanoScience. https://www.nanoscience.com/wp-content/uploads/2023/03/INTRODUCTION-TO-METAL-COATING-TECHNOLOGY-FOR-ELECTRON-MICROSCOPY-compressed-1.pdf.
61. *Application of Time-of-Flight Secondary Ion Mass Spectrometry (ToF-SIMS) in forensic science – A review.* Mackiewicz, E. et al. 2025, Forensic Science International, Vol. 367.
62. *ToF-SIMS - an Overview.* Vickerman, J.
63. *Time-of-flight secondary ion mass spectrometry (TOF-SIMS):—versatility in chemical and imaging surface analysis.* Sodhi, R.N.S. Analyst.
64. *6 - Characterisation of biomedical coatings.* Yaseen, M. et al.
65. TOF-SIMS Technique. *IONTOF.* [Online] https://www.iontof.com/tof-sims-secondary-ion-mass-spectrometry-leis-technique-low-energy-ion-scattering.html.
66. *Review: Recent advances of ToF-SIMS for environmental analysis and imaging.* Shen, Y. et al.
67. Lee, Y.-J. *Mass Spectrometry Imaging of Small Molecules.* s.l. : Humana Press, 2022.
68. *Back to the basics of time-of-flight secondary ion mass spectrometry of bio-related samples. I. Instrumentation and data collection.* Graham, J.D. and Gamble, J.L. 2023.
69. *Enhanced imaging of developed fingerprints and its contaminated substance using ToF-SIMS.* Man, H. et al. 2024.
70. *Targeted ToF-SIMS Analysis of Macrophage Content from a Human.* Malmberg, P. et al. 2021, ACS Applied Bio Materials.
71. *Biological tissue sample preparation for time-of-flight secondary ion mass spectrometry (ToF–SIMS) imaging.* Yoon, S. and Lee, T.G.
72. *Orbitrap™-SIMS analysis of advanced semiconductor inorganic structures.* Franquet, A. et al. 2022, Vacuum, Vol. 202.
73. *Coupling liquid chromatography to Orbitrap mass spectrometry.* Makarov, A. and Scigelova, M. 2010, Journal of Chromatography A, Vol. 1217.

74. *1.50 - Mass Spectrometry.* Perreault, H. and Lattova, E. 2011, Comprehensive Biotechnology.
75. Brydson, J.A. *Plastics Materials.*
76. Poly(methyl acrylate) solution. *SigmaMerck.* [Online] https://www.sigmaaldrich.com/GB/en/product/aldrich/182214.
77. *Acrylate and Methacrylate Polymers' Applications: Second Life with Inexpensive and Sustainable Recycling Approaches.* Corsaro, C. et al.
78. *Fiji: an open-source platform for biological-image analysis.* Schindelin, J. et al. 2012, Nature Methods, Vol. 9, pp. 676-682.
79. *The impact of electrostatic charge in pharmaceutical powders with.* Karner, S. and Urbanetz, N.A. 2011, Journal of Aerosol Science.
80. *A review of factors affecting electrostatic charging of pharmaceuticals and adhesive mixtures for inhalation.* Waseem, K. 2016, International Journal of Pharmaceutics.
82. Lubricants – Pharmaceutical Excipients. *Pharma Excipients* . [Online] https://www.pharmaexcipients.com/lubricants/.
83. Magnesium Sterate. *PubChem.* [Online] 2004. https://pubchem.ncbi.nlm.nih.gov/compound/Magnesium-stearate.
84. Microcrystalline Cellulose. *PubChem.* [Online] https://pubchem.ncbi.nlm.nih.gov/compound/Microcrystalline-Cellulose.
85. Sputter Coaters / Vacuum Coating Systems. *Torontech.* [Online] https://www.torontech.com/sputter-coaters-vacuum-coating-systems/.
86. Principle of Sputter coater: How it works explained. [Online] https://elementpi.com/sputter-coater-principle/.
87. How Does Coating Thickness Affect SEM Imaging? *NanoScience.* [Online] https://www.nanoscience.com/blogs/how-does-coating-thickness-affect-sem-imaging/.
88. Sputter and Carbon coater. *Mascotek Scientific.* [Online] https://mascotekscientific.com/sem-sputter-and-carbon-coater/.
89. *SEM-EDX analysis and TOF-SIMS 3D imaging of a textile/rubber interface undergoing fatigue loading.* C.Valatin, R.Benoit, M.P.D et al. 2016, Applied surface science, Vol. 360.
90. *A critical review of spray-dried amorphous pharmaceuticals: Synthesis, analysis and application.* Wang, B. et al. 2021, International Journal of Pharmaceutics, Vol. 594.
91. *Advancements in ToF-SIMS imaging for life sciences.* Jia, F. et al. 2023.
92. *Assessing the potential of ToF-SIMS as a complementary approach to investigate cement-based materials — Applications related to alkali–silica reaction.* Bernard, L. and Leemann, A. 2015, Cement and Concrete Research, Vol. 68.
93. *Cell and Tissue Imaging by TOF-SIMS and MALDI-TOD: An Overview for Biological and Pharmaceutical Analysis.* Noun, M. et al. 1, s.l. : Microscopy and Microanalysis, 2022, Vol. 26.
94. *Chapter 2 - Physicochemical characterization of microcrystalline cellulose extracted by sequential dual acid hydrolysis.* Kalita, R.D. et al. 2024, Advanced Biophyical Techniques for Polysaccharides Characterization.
95. *Chapter 2 - The development of a pharmaceutical oral solid dosage forms.* Shaikh, R. et al. 2018, Computer Aided Chemical Engineering, Vol. 41.

96. *Characterization and evaluation of varieties of microcrystalline cellulose in formulations containing lactose incompatible drugs: Influence on compactibility and drug release.* Upadhye, A. and M.M, Panday. 2025, International Journal of Biological Macromolecules, Vol. 322.
97. *Discovery pharmaceutics - Challenges and opportunities.* XQ, C. et al. 46, s.l. : AAPS, 206, Vol. 8.
98. *Image and Spectral Processing for ToF-SIMS Analysis of Biological Materials.* Graham, D.J. and Castner, D.G. s.l. : The Mass Spectrometry Society of Japan, 2013. S0014.
99. *Magnesium stearate, a widely-used food additive, exhibits a lack of in vitro and in vivo genotoxic potential.* Hobbs, C.A. et al. 2017, Toxicology reports.
100. *Nano-particles size measurement based on semantic segmentation via convolution neural network.* Zahedi, R. et al. 2025, Measurement, Vol. 240.
101. *Pharmaceutical Application of Tablet Film Coating.* Seo, K.-S et al. 2020, Pharmaceutics.
102. *Pharmaceutical Coating and Its Different Approaches, a Review.* Salawi, A. 2022.
103. *Understanding the Effect of API Properties on Bioavailability Through Absorption Modeling.* Kesisoglou, F. and Wu, Y. 2008, AAPS J.
104. Mansour, H. What Dead Time you should choose for your EDS / EDX analysis? *Oxford Instruments.* [Online] 2022. https://www.oxinst.com/blogs/what-dead-time-you-should-choose-for-your-eds-/-edx-analysis.

Appendix

A1: Excipient blend

For the excipient blend, four different excipients widely used in the pharmaceutical industry are combined. The following excipients are MCC, SGG, DCPA and MgSt. Equal parts of each excipient were poured in a mortar, then evenly combined with a pestle before being transferred into an airtight container.

A2: ImageJ to quantify charging on imaged surface.

To derive the correction factor (in pixels) for the SEM information bar, the mean pixel count of the bar was calculated from images acquired at the lowest acceleration voltage, selected because visual inspection indicated minimal charging across samples under those conditions. During the subsequent quantification of charging, different intensity thresholds were applied at various stages of the thesis to reflect modality- and dataset-specific considerations.

It is important to note that the SEM settings bar appeared completely white and therefore produced a pixel signal. To correct this, the number of pixels within the settings bar was calculated by applying a threshold of 255 for both the lower and upper limits, ensuring that only pixels belonging to the SEM bar were measured.

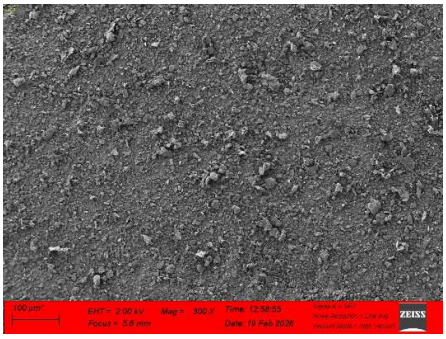

The measured pixels can be obtained from the ImageJ software. This was conducted on all images obtained at 2 kV. Where for each PMA thickness a technical replicate of 3 was used to ensure a better result. The measured pixels for the bar are found in the table below.

Sample ID	Image 1	Image 2	Image 3
A	66542	66499	66503
B	66508	66483	66505
C	66486	66478	66551
D	66463	66478	66490
E	66470	66468	66478

The overall pixels for the entire image were measured by setting the threshold values to:

Upper threshold	255
Lower threshold	0

This resulted in 786432 pixels for all images.

A3: Correction of measured pixels from ImageJ

From the measured pixels for the SEM bar an overall mean value was calculated by using the equation (1).

$$(1)\ Mean = \frac{\sum Measured\ pixels\ for\ SEM\ bar}{Amount\ of\ measured\ locations} = \frac{997402}{15} = 66493.47$$

This mean value would be used in the further calculations when correcting the amount of charging in % with relation to the SEM bar settings which increases the charging value due to being completely white, since white is the indication of charging on SEM image. Therefore, the assumption would be that the SEM bar has the same number of pixels for each image. To measure the percentage of charging the equation (2) was used.

$$(2)\ Charged\ \% = \frac{Amount\ of\ pixels\ measured\ with\ selected\ threshold - the\ mean\ value\ of\ SEM\ bar}{Total\ amount\ of\ pixels\ in\ the\ image}$$

With both the number of pixels measured for the charging prospect but also for the overall image the mean value of the SEM bar was subtracted to correct the values against this.

A4: Example calculations of charging% from ImageJ output

Voltage	**Counts (AP)**	**Counts / total counts**	**Charging %**	**Counts (BP)**	**Counts / total counts**	**Charging %**
2	75545	0.096	9.6%	69583	0.088	8.8%
2	76417	0.097	9.7%	71416	0.091	9.1%
2	77913	0.099	9.9%	69467	0.088	8.8%
Mean 2kV	76625	0.097	9.7%	70155.33	0.089	8.9%
3	253556	0.322	32.2%	329569	0.419	41.9%
3	283448	0.360	36.0%	240389	0.306	30.6%
3	349416	0.444	44.4%	75268	0.096	9.6%
Mean 3kv	295473.3	0.376	37.6%	215075.3	0.273	27.3%
4	369419	0.470	47.0%	306613	0.390	39.0%
4	395583	0.503	50.3%	287117	0.365	36.5%
4	576552	0.733	73.3%	285820	0.363	36.3%
Mean 4 kV	447184.7	0.569	56.9%	293183.3	0.373	37.3%
5	547612	0.696	69.6%	452848	0.576	57.6%
5	507372	0.645	64.5%	493039	0.627	62.7%
5	579916	0.737	73.7%	474704	0.604	60.4%
Mean 5 kV	544966.7	0.693	69.3%	473530.3	0.602	60.2%

Voltage	Counts (CP)	Counts / total counts	Charging %	Counts (DP)	Counts / total counts	Charging %	Counts (EP)	Counts / total counts	Charging %
2	72860	0.093	9.3%	75428	0.096	9.6%	72015	0.092	9.2%
2	74859	0.095	9.5%	78550	0.100	10.0%	72313	0.092	9.2%
2	71603	0.091	9.1%	78553	0.100	10.0%	72469	0.092	9.2%
Mean 2 kV	73107.3	0.093	9.3%	77510.33	0.099	9.9%	72265.67	0.092	9.2%
3	108700	0.138	13.8%	76583	0.097	9.7%	72356	0.092	9.2%
3	97907	0.124	12.4%	76386	0.097	9.7%	72451	0.092	9.2%
3	124404	0.158	15.8%	76319	0.097	9.7%	74477	0.095	9.5%
Mean 3 kV	110337	0.140	14.0%	76429.33	0.097	9.7%	73094.67	0.093	9.3%
4	84963	0.108	10.8%	79962	0.102	10.2%	74547	0.095	9.5%
4	92670	0.118	11.8%	80703	0.103	10.3%	81805	0.104	10.4%
4	71737	0.091	9.1%	82450	0.105	10.5%	76015	0.097	9.7%
Mean 4 kV	83123.3	0.106	10.6%	81038.33	0.103	10.3%	77455.67	0.098	9.8%
5	76248	0.097	9.7%	93238	0.119	11.9%	89333	0.114	11.4%
5	104251	0.133	13.3%	103183	0.131	13.1%	91687	0.117	11.7%
5	76579	0.097	9.7%	90905	0.116	11.6%	84663	0.108	10.8%
Mean 5 kV	85692.7	0.109	10.9%	95775.33	0.122	12.2%	88561	0.113	11.3%
6	157787	0.201	20.1%	108218	0.138	13.8%	108651	0.138	13.8%
6	82652	0.105	10.5%	139960	0.178	17.8%	106658	0.136	13.6%
6	84186	0.107	10.7%	113313	0.144	14.4%	147379	0.187	18.7%
Mean 6 kV	108208.3	0.138	13.8%	120497	0.153	15.3%	120896	0.154	15.4%
7	83743	0.106	10.6%	118963	0.151	15.1%	139517	0.177	17.7%
7	138087	0.176	17.6%	128718	0.164	16.4%	208599	0.265	26.5%
7	89132	0.113	11.3%	122552	0.156	15.6%	187786	0.239	23.9%
Mean 7 kV	103654	0.132	13.2%	123411	0.157	15.7%	178634	0.227	22.7%
8	103011	0.131	13.1%	127343	0.162	16.2%	170045	0.216	21.6%
8	99642	0.127	12.7%	154558	0.197	19.7%	208744	0.265	26.5%
8	108834	0.138	13.8%	129707	0.165	16.5%	212940	0.271	27.1%
Mean 8 kV	103829	0.132	13.2%	137202.7	0.174	17.4%	197243	0.251	25.1%
9	105455	0.134	13.4%	165936	0.211	21.1%	178549	0.227	22.7%
9	99584	0.127	12.7%	132776	0.169	16.9%	217075	0.276	27.6%
9	99165	0.126	12.6%	206091	0.262	26.2%	195326	0.248	24.8%
Mean 9 kV	101401.3	0.129	12.9%	168267.7	0.214	21.4%	196983.3	0.250	25.0%
10	107629	0.137	13.7%	129370	0.165	16.5%	187796	0.239	23.9%
10	113692	0.145	14.5%	191506	0.244	24.4%	198800	0.253	25.3%
10	141894	0.180	18.0%	162632	0.207	20.7%	211977	0.270	27.0%
Mean 10 kV	121071.7	0.154	15.4%	161169.3	0.205	20.5%	199524.3	0.254	25.4%

A5: Placement of sample in SEM holder

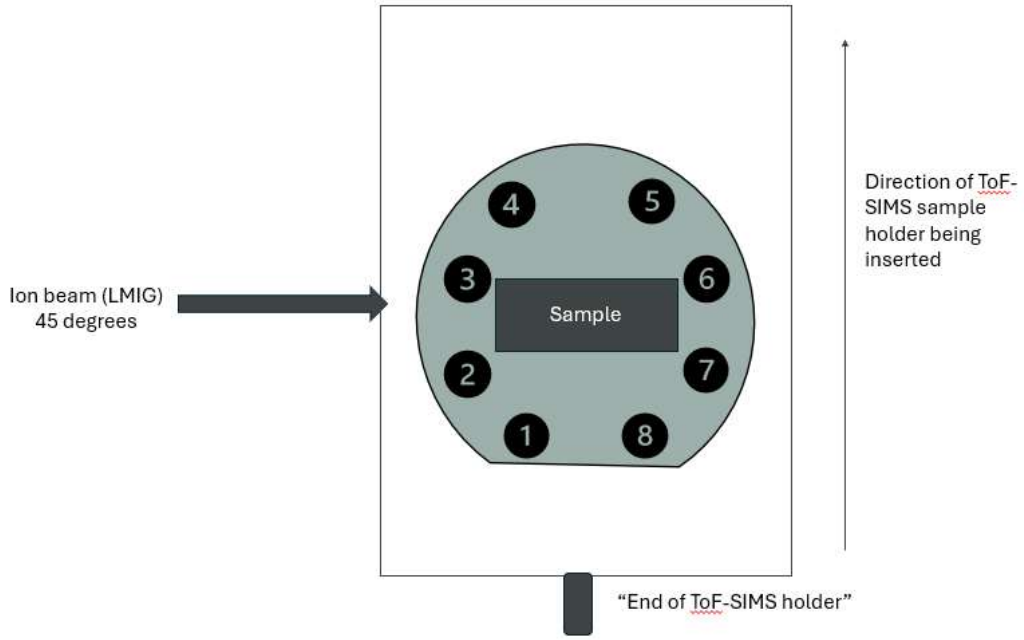

By placing the sample with the direction of the ion beam in ToF-SIMS to the side with the lower numbers, the tilting would result in the same direction. The stage was placed at a rotation of 285°, this would generate in the side with lower numbers being tilted upwards against the electron beam.

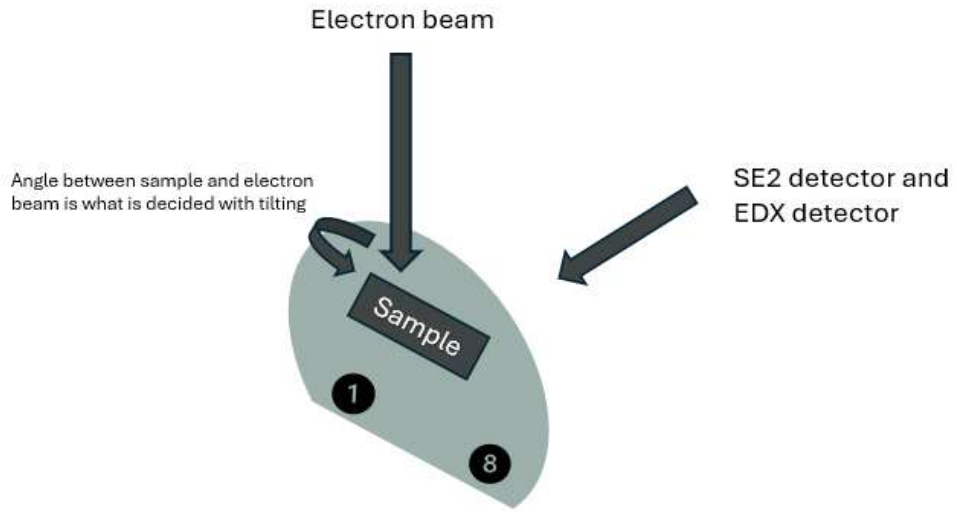

A6: Images of CP before and after EDX at different acceleration voltages

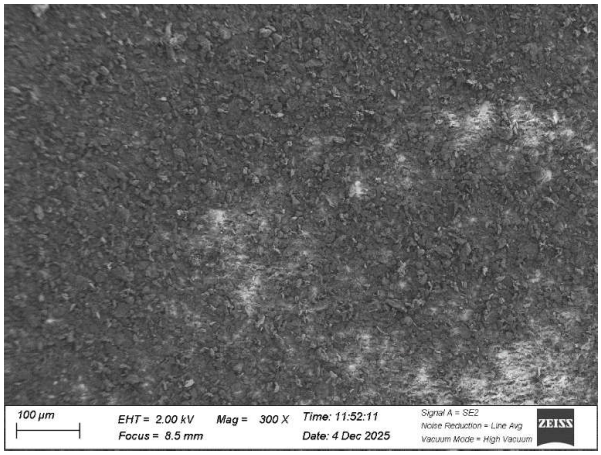

(a): Before EDX at 2 kV

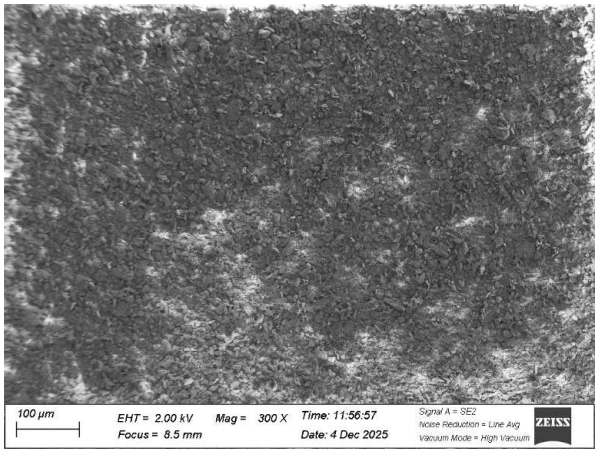

(b): After EDX at 2 kV

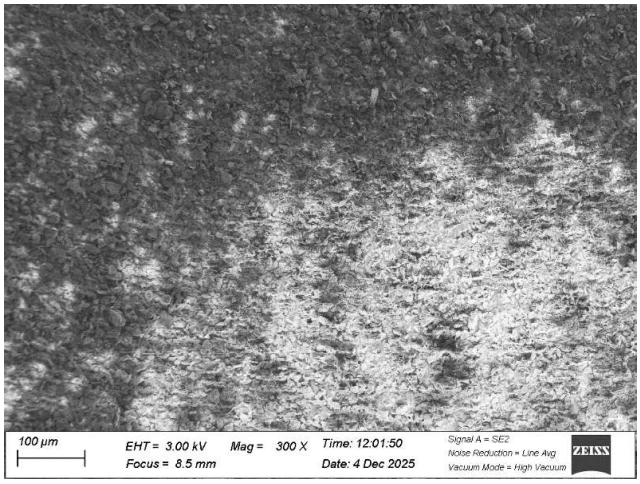

(a): Before EDX at 3 kV

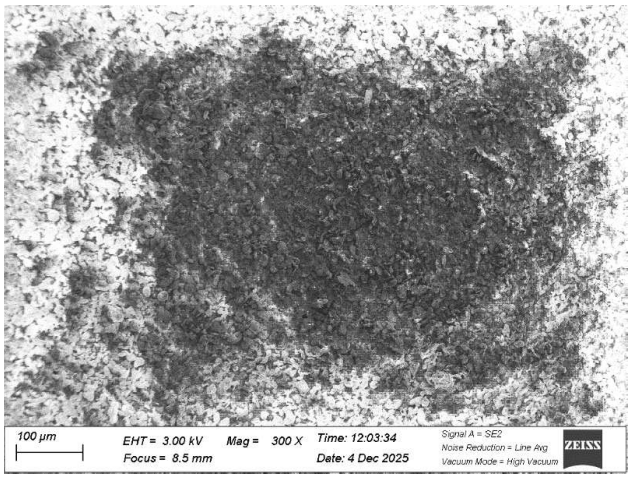

(b): After EDX at 3 kV

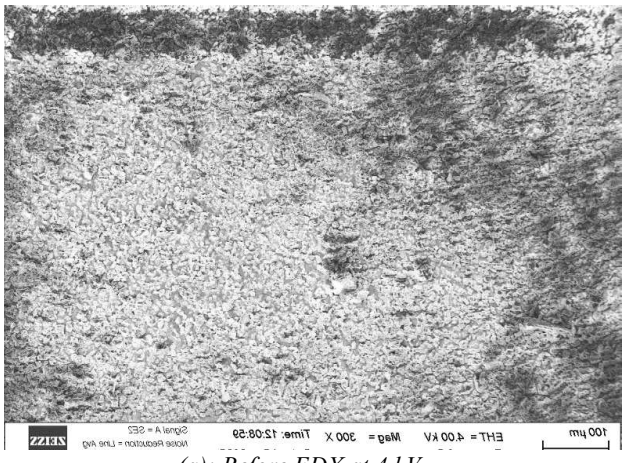

(a): Before EDX at 4 kV

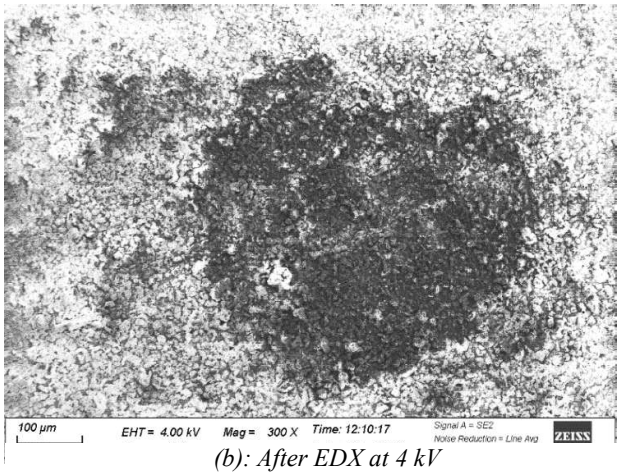

(b): After EDX at 4 kV

A7: Elemental maps Excipients on PMA C at 5 kV

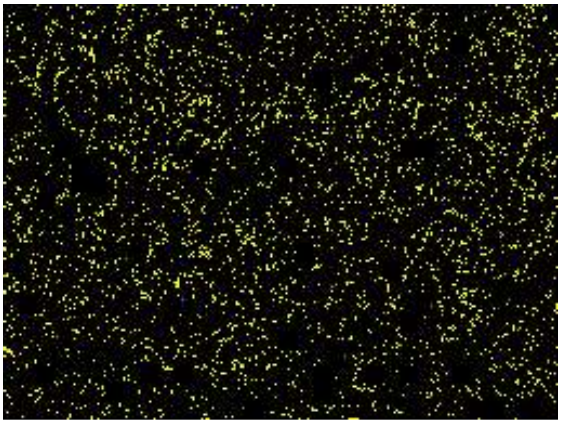

Al

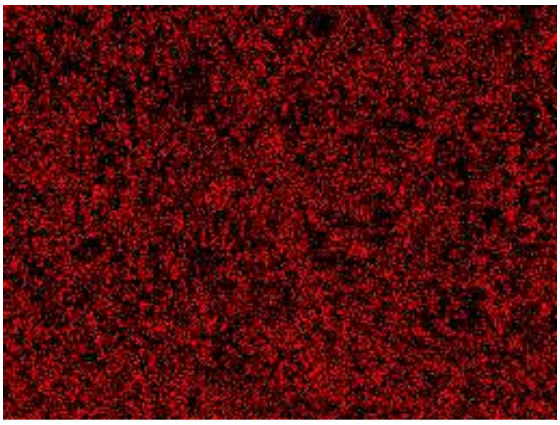

C



P

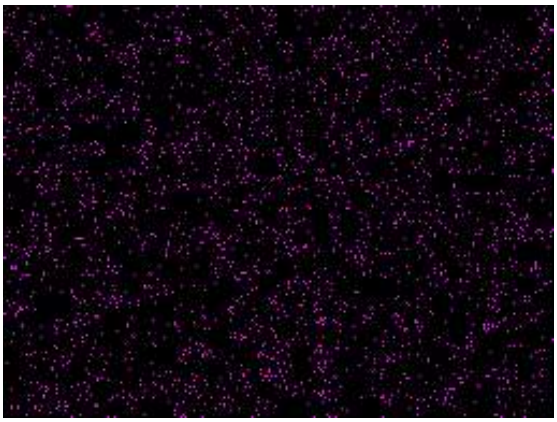

Mg

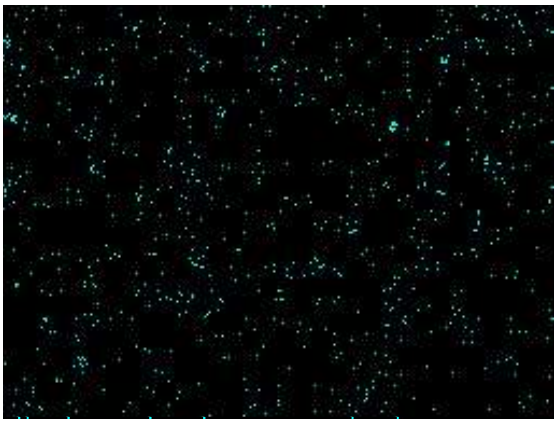

Na

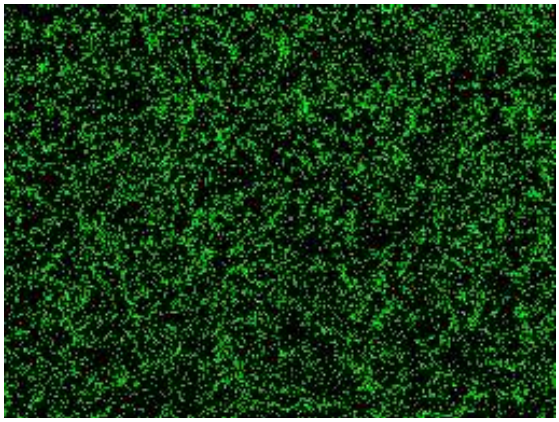

O

A8: Elemental maps Excipients on PMA C at 15 kV in VP mode

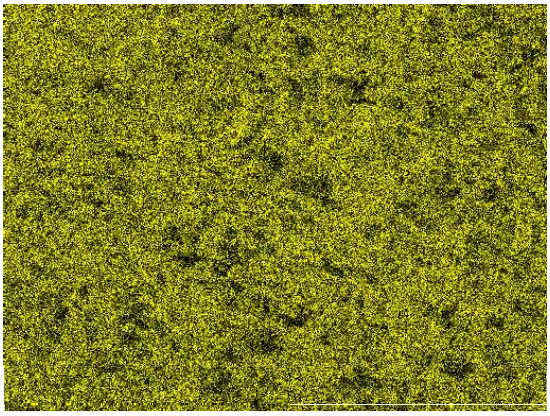

Al

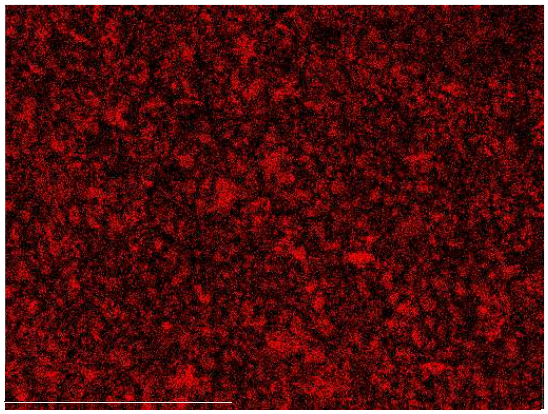

C

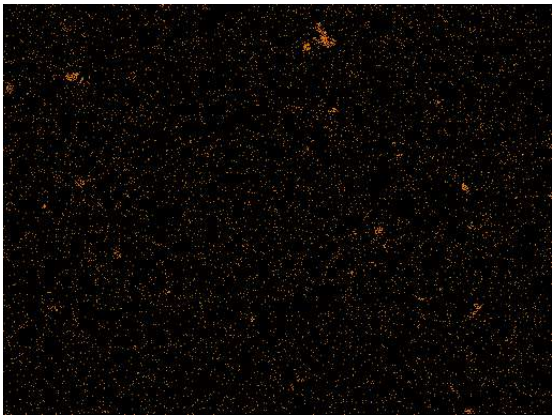

P

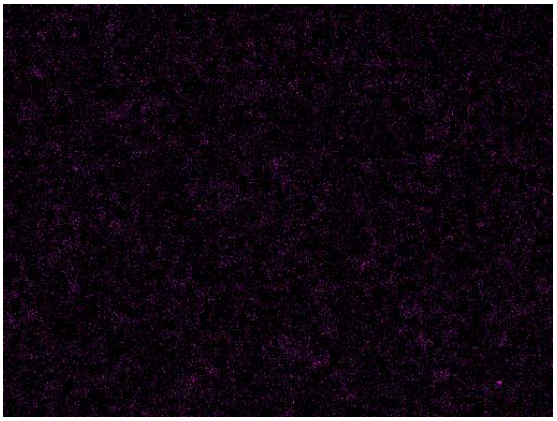

Mg

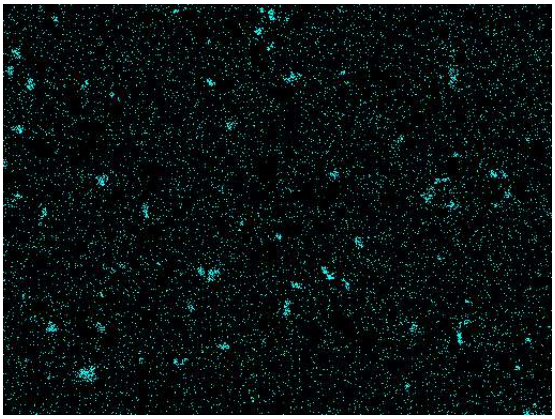

Na

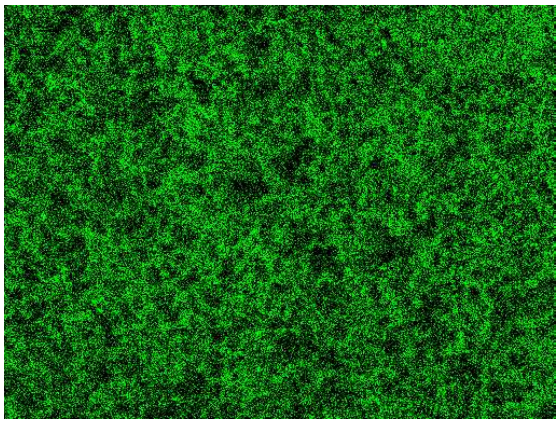

O

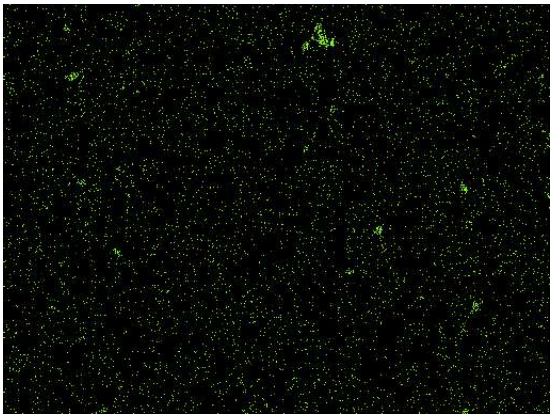

Ca

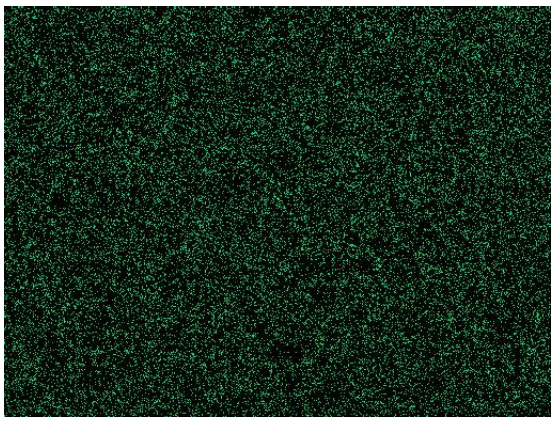

S

A9: Elemental composition of spray-dried powder at different kV in VP mode

	Wt% 5 kV	Standard deviation	Wt% 7 kV	Standard deviation	Wt% 8 kV	Standard deviation
Carbon	69.59	0.42	72.24	0.18	68.36	0.26
Nitrogen	2.59	0.3	0	0.44	1.51	0.29
Oxygen	23.33	0.25	23.97	0.16	25.83	0.17
Sodium	1.1	0.07	1.02	0.05	1.13	0.04
Phosphorus	1.52	0.13	1.27	0.07	1.49	0.06
Sulfur	1.52	0.16	1.5	0.08	1.59	0.06
Silicon	0.24	0.08	0	0	0.09	0.03
Potassium	0.09	0.31	0	0	0	0

A10: Elemental composition of cluster on AP sample at different working distances

	Wt% at WD 8.5 mm	Standard deviation	Wt% at WD 5.0 mm	Standard deviation
Carbon	63.74	0.14	65.71	0.18
Oxygen	27.27	0.13	25.67	0.16
Sodium	1.05	0.03	1.18	0.04
Magnesium	2.06	0.03	2.23	0.04
Aluminum	4.12	0.05	3.2	0.05
Phosphorus	0.55	0.03	0.06	0.04
Sulfur	0.43	0.03	0.37	0.04
Chloride	0.24	0.03	0.36	0.04
Calcium	0.56	0.04	0.69	0.06

A11: Elemental composition of different PMA thicknesses at 3 kV

	Wt% AP	Wt% BP	Wt% CP	Wt% DP	Wt% EP	Wt% No PMA
Carbon	78.3	79.21	64.78	72.23	69.68	79.63
Oxygen	17.17	16.66	23.28	19.34	21.18	15.85
Sodium	0.42	0.25	0.73	0.52	0.26	1.02
Magnesium	3.39	3.89	3.2	3.79	3.92	1.9
Aluminium	0	0	8	4.11	4.97	0
Phosphourus	0.73	0	0.01	0.01	0	0.65
Silicon	0	0	0	0	0	0.95

A12: Visual Observation of the charging on PMA A (AP) and PMA E (EP) at 5 kV

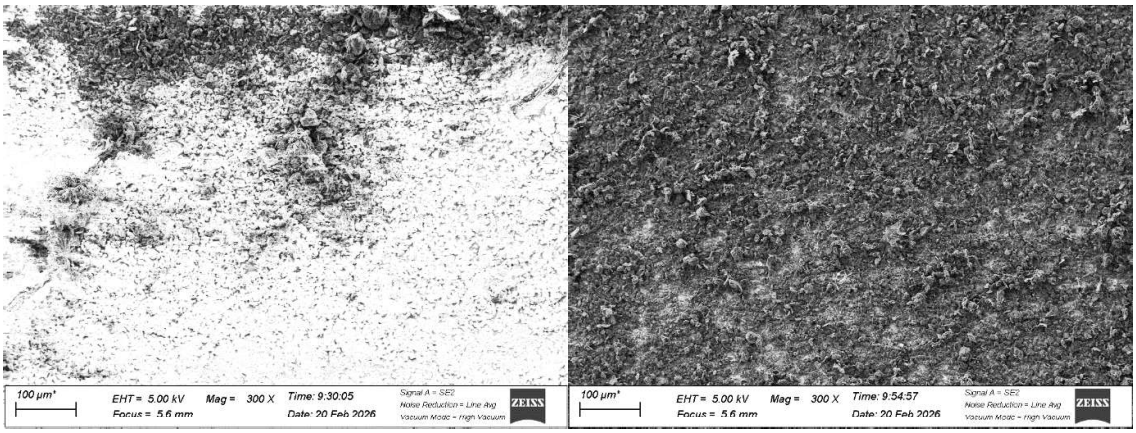

PMA thickness A PMA thickness E

A13: Different angles evaluated with SEM

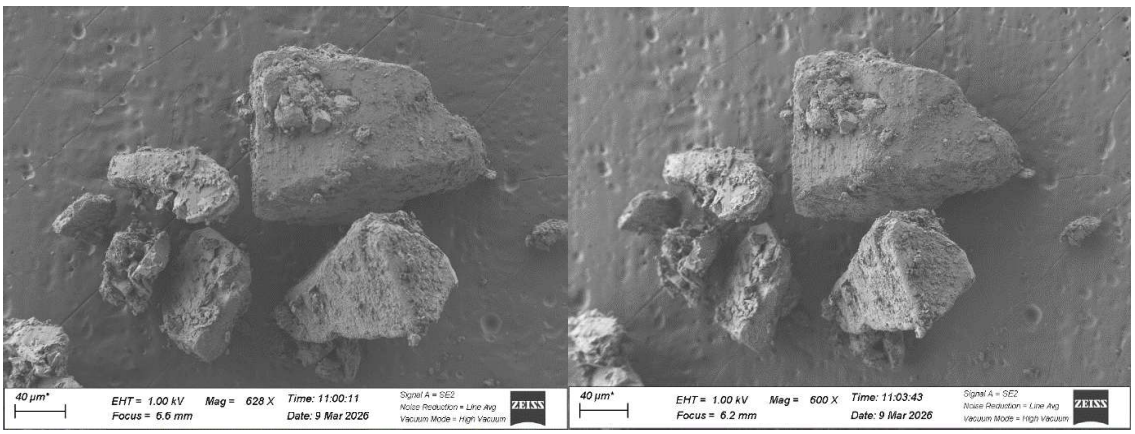

0 º 15º

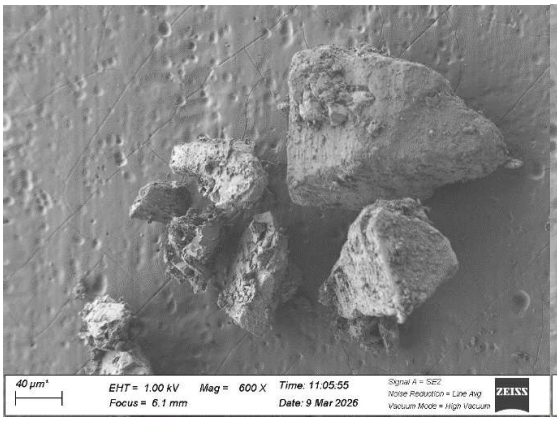

20º

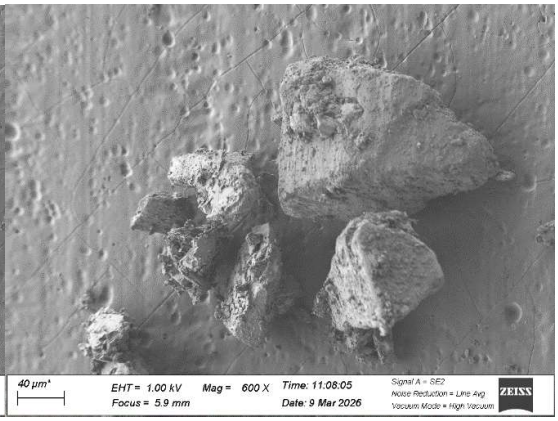

25º

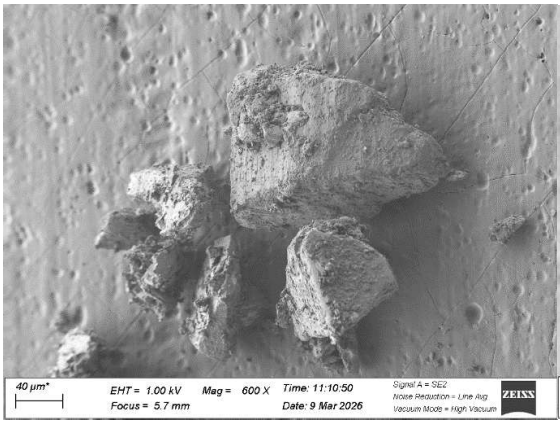

30º

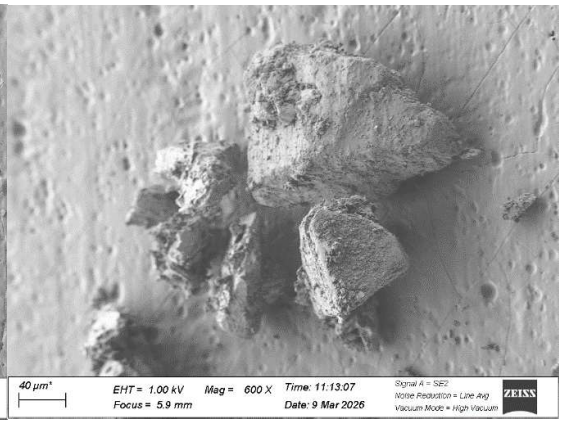

35º

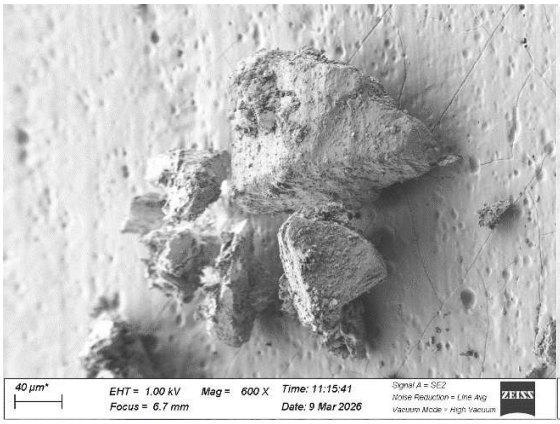

40º

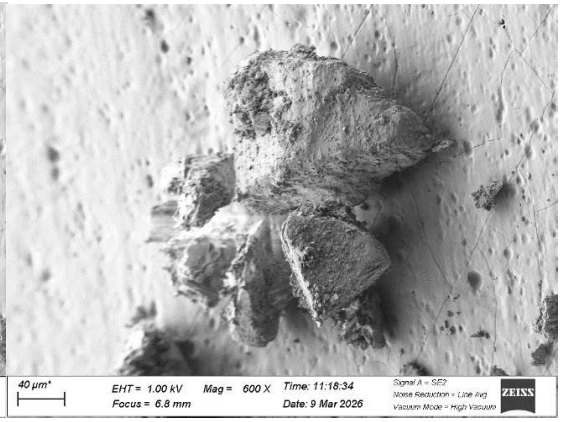

45º

A14: Elemental maps of the skin model (SEM-EDX)



Al

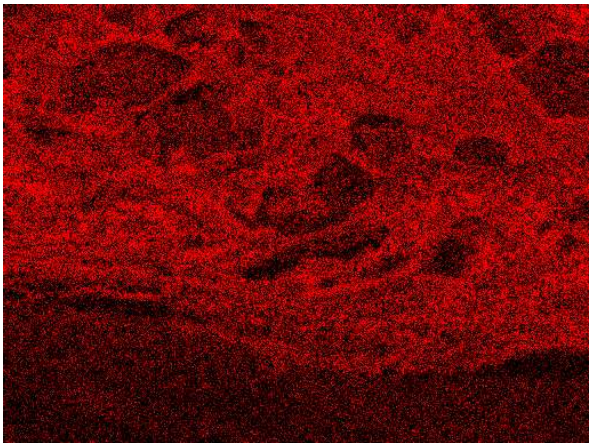

C

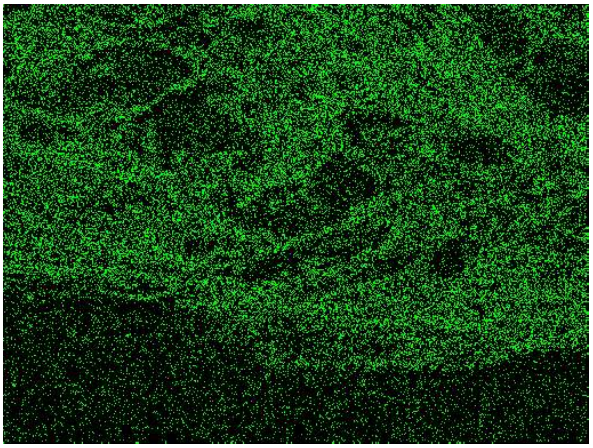

O

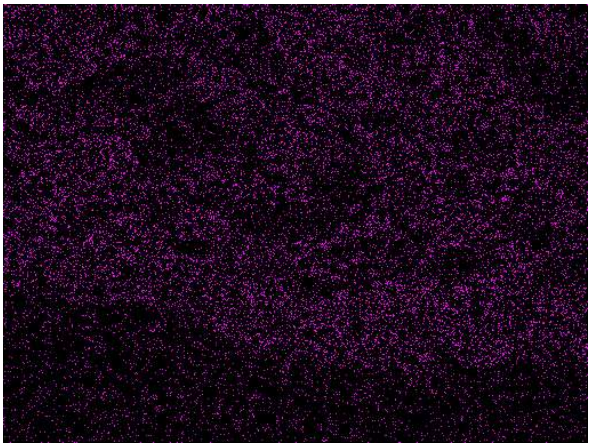

Cl

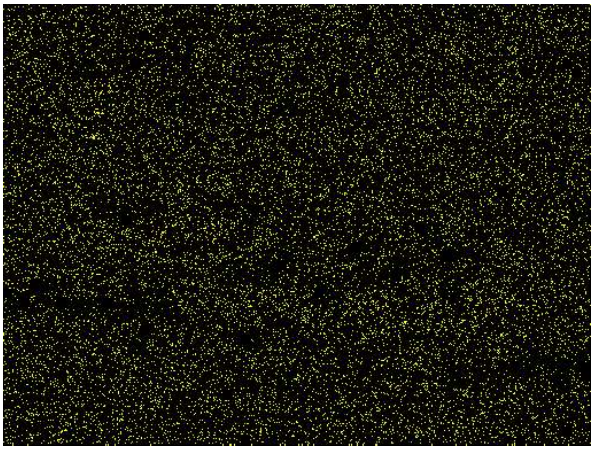

Na

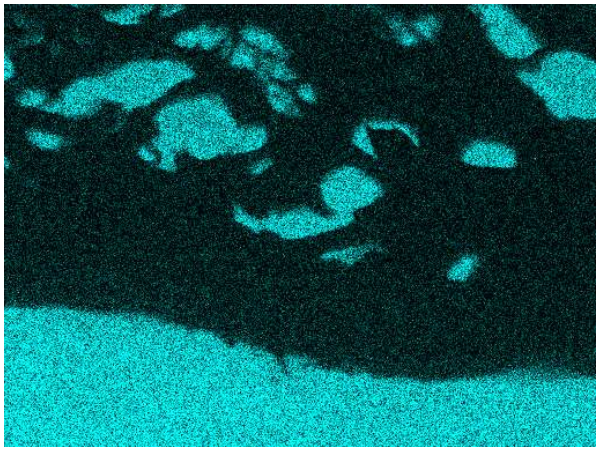

Si

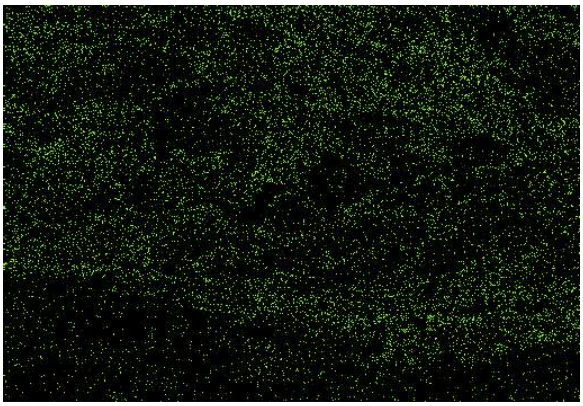

N

DEPARTMENT OF LIFE SCIENCE
CHALMERS UNIVERSITY OF TECHNOLOGY
Gothenburg, Sweden 2026
www.chalmers.se



CHALMERS
UNIVERSITY OF TECHNOLOGY